



# On High Order ADER Discontinuous Galerkin Schemes for First Order Hyperbolic Reformulations of Nonlinear Dispersive Systems

Saray Busto<sup>1</sup> · Michael Dumbser<sup>1</sup> · Cipriano Escalante<sup>2</sup> · Nicolas Favrie<sup>3</sup> ·  
Sergey Gavriluk<sup>3,4</sup>

Received: 14 December 2020 / Revised: 23 January 2021 / Accepted: 8 February 2021 /  
Published online: 25 March 2021  
© The Author(s) 2021

## Abstract

This paper is on arbitrary high order fully discrete one-step ADER discontinuous Galerkin schemes with subcell finite volume limiters applied to a new class of first order hyperbolic reformulations of nonlinear dispersive systems based on an extended Lagrangian approach introduced by Dhaouadi et al. (Stud Appl Math 207:1–20, 2018), Favrie and Gavriluk (Nonlinearity 30:2718–2736, 2017). We consider the hyperbolic reformulations of two different nonlinear dispersive systems, namely the Serre–Green–Naghdi model of dispersive water waves and the defocusing nonlinear Schrödinger equation. The first order hyperbolic reformulation of the Schrödinger equation is endowed with a curl involution constraint that needs to be properly accounted for in multiple space dimensions. We show that the original model proposed in Dhaouadi et al. (2018) is only *weakly hyperbolic* in the multi-dimensional case and that strong hyperbolicity can be restored at the aid of a novel thermodynamically compatible GLM curl cleaning approach that accounts for the curl involution constraint in the PDE system. We show one and two-dimensional numerical results applied to both systems and compare them with available exact, numerical and experimental reference solutions whenever possible.

**Keywords** High order ADER discontinuous Galerkin schemes with subcell finite volume limiter · Hyperbolic reformulations of nonlinear dispersive systems · Well-balancing · Curl involution constraint · Thermodynamically compatible GLM curl cleaning · Serre–Green–Naghdi model · Nonlinear Schrödinger equation

---

✉ Saray Busto  
saray.busto@unitn.it

✉ Michael Dumbser  
michael.dumbser@unitn.it

<sup>1</sup> Department of Civil, Environmental and Mechanical Engineering, University of Trento, Via Mesiano 77, 38123 Trento, Italy

<sup>2</sup> Department of Mathematics, University of Cordoba, 14071 Córdoba, Spain

<sup>3</sup> Aix-Marseille Univ and CNRS UMR 7343 IUSTI, 5 rue Enrico Fermi, 13453 Marseille, France

<sup>4</sup> Lavrentyev Institute of Hydrodynamics, 15 Lavrentyev Ave., Novosibirsk, Russia 630090

## 1 Introduction

Nonlinear dispersive systems can be found in many different areas of computational mechanics, ranging from large scale dispersive free surface shallow water flows [12,28,62,87,93,94] over multi-phase flows with surface tension [13,39] down to quantum fluid mechanics [14,15,65,75]. A common difficulty in the above applications is that the nonlinear time-dependent governing partial differential equations (PDE) typically contain either higher order spatial and temporal derivatives, or a subset of elliptic equations, and therefore the integration with simple explicit finite volume and discontinuous Galerkin finite element schemes becomes unfeasible.

Therefore, very recently, there has been an increasing interest in *rewriting* nonlinear PDE systems with higher order derivatives under the form of nonlinear hyperbolic relaxation systems, which contain at most first order derivatives in space and time, in conjunction with potentially stiff algebraic relaxation source terms. The idea goes back to the seminal work of Cattaneo [25], who proposed a hyperbolic reformulation of the parabolic heat equation. More recent work on the topic also regards the hyperbolic reformulation of advection-diffusion equations [80,84,85,99], of the compressible Navier-Stokes equations [17,47,88] as well as hyperbolic reformulations of nonlinear dispersive systems [3,4,26,51,52,63,64,79,90]. We would like to point out a particularity of the hyperbolic dispersive system proposed in [3], since it can be derived from the depth averaged *compressible* Euler equations, while most depth-averaged shallow water systems are usually derived from the governing equations of an *incompressible* fluid. Also the well-known theory of rational extended thermodynamics [82] makes use of hyperbolic relaxation systems to model the effects of higher order derivative terms.

In this paper we focus in particular on the hyperbolic reformulation of the Serre–Green–Naghdi model introduced by Favrie and Gavrilyuk in [56], as well as on the hyperbolic reformulation of the nonlinear defocusing Schrödinger equation proposed by Dhaouadi *et al.* in [38]. Both systems were rigorously derived from an extended Lagrangian formalism and therefore have a rather similar mathematical structure. The hyperbolic reformulation of the nonlinear Schrödinger equation [38] has the additional difficulties that it is only weakly hyperbolic in multiple space dimensions and that it is endowed with a *curl invariance constraint* that needs to be properly accounted for. In this paper we will make use of the hyperbolic generalized Lagrangian multiplier (GLM) curl cleaning approach of [27,46] that goes back to the hyperbolic GLM divergence cleaning technique of Munz *et al.* for Maxwell and MHD equations, see [35,83]. In alternative to the GLM method proposed here, also exactly curl-preserving schemes could be used, see e.g. [1,11,27,66,67,71], but they require an appropriately staggered mesh and are therefore not as easy to implement in an existing general purpose DG solver as the simple GLM method, which only requires the solution of additional PDEs for the cleaning quantities. The main novelty proposed in the present paper is a new GLM curl cleaning that is also *thermodynamically compatible* with the conservation of total energy.

To integrate the governing PDE systems under consideration in this paper we will make use of high order accurate *explicit* discontinuous Galerkin (DG) finite element schemes. The DG framework for hyperbolic conservation laws goes back to the seminal work of Cockburn and Shu [29–32] and was later generalized to hyperbolic equations with parabolic terms in [5,6,33,34]. The first extension of DG schemes to dispersive PDE of the Korteweg–de Vries (KdV) type with up to third order spatial derivatives was achieved in [106,107], while DG schemes for PDE with even higher order spatial derivatives were first tackled in

[70]. Discontinuous Galerkin finite element schemes for the solution of nonlinear dispersive Boussinesq-type equations were forwarded in [50,54,55]. To overcome the very severe time step restriction of explicit DG schemes applied to dispersive equations, which require the time step to scale with the cube of the mesh spacing ( $\Delta t \propto \Delta x^3$ ), see [106], fully implicit space-time DG schemes for dispersive problems were introduced in [45]. However, although the resulting schemes are unconditionally stable they are computationally very expensive due to the ill-conditioned algebraic systems that must be solved in each time step. For this reason, in this work we prefer the numerical solution of hyperbolic reformulations of nonlinear dispersive systems, which allow the straightforward use of simple explicit DG schemes for hyperbolic PDE with the usual CFL-type time step restriction, according to which the time step must be chosen proportional to the mesh spacing ( $\Delta t \propto \Delta x$ ), rather than more complex implicit DG schemes for PDE with higher order derivatives. In alternative to high order DG methods, also high order residual distribution (RD) schemes can be applied to Boussinesq-type equations, see [90].

The rest of this paper is structured as follows: in Sect. 2 we present the two nonlinear dispersive models that we want to study, namely the hyperbolic reformulation of the Serre–Green–Naghdi system of dispersive free surface water waves forwarded by Favrie and Gavriluyk in [56] and the hyperbolic reformulation of the nonlinear defocusing Schrödinger equation proposed by Dhaouadi *et al.* in [38]. Compared to the original work on the hyperbolic reformulation of the Serre–Green–Naghdi system [56] in this paper we also add the *bottom slope term* and design an exactly *well-balanced* numerical scheme for the resulting system that is capable of preserving stationary lake at rest solutions exactly at the discrete level for arbitrary bottom topography. Compared to the work on the hyperbolic reformulation of the Schrödinger equation [38] in this paper an additional term is added to the system in order to restore *Galilean invariance* and also the *curl involution constraint* of the system is explicitly taken into account, which is necessary for the multi-dimensional case. As already mentioned previously, in this paper we will make use of a hyperbolic generalized Lagrangian multiplier (GLM) approach, see [27,35,46,83], which also restores strong hyperbolicity of the system.

In Sect. 3 we present the framework of arbitrary high order derivative (ADER) discontinuous Galerkin finite element schemes used for the numerical solution of the hyperbolic governing PDE systems. Section 4 is devoted to the presentation and discussion of the numerical results obtained for both systems. Wherever possible, we compare with exact, numerical or experimental reference solutions. In Sect. 5 we draw some conclusions and give an outlook to future research.

## 2 Governing Equations

Throughout this paper we will make use of the Einstein summation convention over two repeated indices. We further denote the time with  $t$  and the Cartesian coordinate axes by  $x_k$  for  $k \in \{1, \dots, d\}$  with  $d$  the number of space dimensions. Sometimes we will also make use of the notation  $x := x_1$ ,  $y := x_2$  and  $\partial_x = \frac{\partial}{\partial x}$ .

### 2.1 A Hyperbolic Reformulation of the Serre–Green–Naghdi Model

The governing PDE system generalizing that proposed in [56] to reformulate the Serre–Green–Naghdi model as a first order hyperbolic system and derived from the extended

Lagrangian variational principle reads as follows (see Appendix A for details):

$$\frac{\partial h}{\partial t} + \frac{\partial}{\partial x_k} (h v_k) = 0, \tag{1}$$

$$\frac{\partial h v_i}{\partial t} + \frac{\partial}{\partial x_k} \left( h v_i v_k + \left( \frac{1}{2} g h^2 + h p \right) \delta_{ik} \right) + \left( g h + \frac{3}{2} \frac{h}{\eta} p \right) \frac{\partial b}{\partial x_i} = 0, \tag{2}$$

$$\frac{\partial h \eta}{\partial t} + \frac{\partial}{\partial x_k} (h \eta v_k) + \frac{3}{2} h v_k \frac{\partial b}{\partial x_k} = h w, \tag{3}$$

$$\frac{\partial h w}{\partial t} + \frac{\partial}{\partial x_k} (h w v_k) = \lambda \left( 1 - \frac{\eta}{h} \right), \tag{4}$$

$$\frac{\partial b}{\partial t} = 0, \tag{5}$$

with the nonhydrostatic pressure  $p(h, \eta) = \frac{\lambda}{3} \frac{\eta}{h} \left( 1 - \frac{\eta}{h} \right)$ , the gravity constant  $g = 9.81 \text{ m}^2/\text{s}$  and where the parameter  $\lambda$  having the dimension  $\text{m}^2/\text{s}^2$  is a large (compared to the squared velocity of surface waves  $gh$ ) free parameter which makes the system (1)–(5) tend to the original Serre–Green–Naghdi model in the limit  $\lambda \rightarrow \infty$ . The rigorous proof of this fact has been established in [40] in the case of flat bottom. Note that for  $\lambda \rightarrow \infty$  the term  $(1 - \eta/h) \rightarrow 0$  since  $\eta \rightarrow h$ , hence the product will remain *finite*. Compared to [56] in system (1)–(5) the mild bottom slope terms are added (see Appendix A for details). The system admits the energy conservation law which is a direct consequence of the Noether theorem.

For a hyperbolic reformulation of the Serre–Green–Naghdi model without mild bottom assumption and directly derived from the compressible Euler equations, the reader is referred to [3]. The derivation from the compressible Euler equations presented in [3] can also be used to establish a connection between the square of the *sound speed* in the compressible medium and the *penalty parameter*  $\lambda$  used in the model (1)–(5). However, the model proposed in [3] is non-conservative even for flat bottom (see also [51,52]). In the rest of this paper we sometimes refer to the model (1)–(5) also as the Favrie–Gavrilyuk (FG) model, since it is the extension of [56] to the case of mildly varying bottom.

### 2.1.1 Eigenstructure

The hyperbolicity of system (1)–(5) was already studied in [56] for the one dimensional case with *flat bottom*, while here we show the results for the two-dimensional situation with *variable bottom*. The eigenvalues of system (1)–(5) in  $x_1$  direction are

$$\lambda_1 = v_1 - a, \quad \lambda_{2,3,4} = v_1, \quad \lambda_5 = v_1 + a, \quad \lambda_6 = 0, \tag{6}$$

with the celerity  $a = \sqrt{gh + \frac{1}{3} \lambda \frac{\eta^2}{h^2}}$  and the associated right eigenvectors

$$\mathbf{r}_1 = \begin{pmatrix} 1 \\ v_1 - a \\ v_2 \\ \eta \\ w \\ 0 \end{pmatrix}, \mathbf{r}_2 = \begin{pmatrix} 0 \\ 0 \\ 0 \\ 0 \\ 1 \\ 0 \end{pmatrix}, \mathbf{r}_3 = \begin{pmatrix} 0 \\ 0 \\ 1 \\ 0 \\ 0 \\ 0 \end{pmatrix}, \mathbf{r}_4 = \begin{pmatrix} 1 \\ v_1 \\ 0 \\ A \\ 0 \\ 0 \end{pmatrix}, \mathbf{r}_5 = \begin{pmatrix} 1 \\ v_1 + a \\ v_2 \\ \eta \\ w \\ 0 \end{pmatrix}, \tag{7}$$

and

$$\mathbf{r}_6 = \left( -\frac{3}{2} \frac{B}{T}, 0, -\frac{3}{2} v_2 \frac{B}{T}, -\frac{3}{2} \frac{C}{T}, -\frac{3}{2} w \frac{B}{T}, 1 \right)^T, \tag{8}$$

with the auxiliary quantities  $A = -\frac{3gh^3 - \lambda h\eta + 3\lambda\eta^2}{\lambda(h-2\eta)}$ ,  $T = 3gh^3 - 3h^2v_1^2 + \eta^2\lambda$ ,  $B = h(2gh^2 + \eta\lambda)$  and  $C = h(2\eta gh^2 + 3gh^3 - 3h^2v_1^2 + 2\eta^2\lambda)$ .

### 2.1.2 Linear Dispersion Analysis and Comparison with Other Hyperbolic Models

Following [3,51,73,77], we carry out a linear dispersion analysis of the system (1)–(5) for flat bottom, ignoring all terms involving  $b$ . To simplify the expressions, we consider only the one-dimensional case and introduce the vector of primitive variables  $\mathbf{V} = (h, u, \eta, w)^T$ . Rewriting of the governing PDE system in terms of the primitive variables leads to

$$\partial_t \mathbf{V} + \mathbf{C}(\mathbf{V}) \partial_x \mathbf{V} = \mathbf{S}(\mathbf{V}) \tag{9}$$

with

$$\mathbf{C}(\mathbf{V}) = \frac{\partial \mathbf{V}}{\partial \mathbf{U}} \frac{\partial \mathbf{F}}{\partial \mathbf{V}}, \quad \text{and} \quad \frac{\partial \mathbf{V}}{\partial \mathbf{U}} = \left( \frac{\partial \mathbf{U}}{\partial \mathbf{V}} \right)^{-1}. \tag{10}$$

After decomposition of the primitive variables into a *stationary* component  $\mathbf{V}_0$  plus a small time-dependent fluctuation  $\mathbf{V}'$  and assuming that  $\mathbf{S}(\mathbf{V}_0) = 0$ , we get the linearised system

$$\partial_t \mathbf{V}' + \mathbf{C}(\mathbf{V}_0) \partial_x \mathbf{V}' = \mathbf{E}(\mathbf{V}_0) \mathbf{V}', \quad \mathbf{E} = \frac{\partial \mathbf{S}}{\partial \mathbf{V}} \tag{11}$$

that can be studied using standard Fourier analysis. The ansatz  $\mathbf{V}'(x, t) = \hat{\mathbf{V}} e^{i(\kappa x - \omega t)}$  with  $i^2 = -1$  leads to

$$\partial_t \mathbf{V}' = -i\omega \mathbf{V}', \quad \partial_x \mathbf{V}' = i\kappa \mathbf{V}'. \tag{12}$$

Hence, from (11), we obtain

$$(-\omega \mathbf{I} + \kappa \mathbf{C}(\mathbf{V}_0) + \mathbf{E}(\mathbf{V}_0) i) \mathbf{V}' = 0. \tag{13}$$

In particular, taking the rest state  $\mathbf{V}_0 = (H, 0, H, 0)$  the linearised matrix related to system (1)–(5) in primitive variables reads

$$\mathbf{M}_0 = \kappa \mathbf{C}(\mathbf{V}_0) + \mathbf{E}(\mathbf{V}_0) i = \begin{pmatrix} 0 & \kappa H & 0 & 0 \\ \kappa g + \frac{1}{3} \frac{\kappa \lambda}{H} & 0 & -\frac{1}{3} \frac{\kappa \lambda}{H} & 0 \\ 0 & 0 & 0 & i \\ \frac{i\lambda}{H^2} & 0 & -\frac{i\lambda}{H^2} & 0 \end{pmatrix}. \tag{14}$$

The eigenvalue problem  $\mathbf{M}_0 \mathbf{V}' = \omega \mathbf{V}'$  can be solved numerically, thus obtaining the phase velocity  $C_p = \frac{\omega}{\kappa}$ . For comparison with other available models in the bibliography, it is important to note that the parameter  $\lambda$  is chosen as  $\lambda = 3c^2 = 3\alpha^2 gH$  with  $c$  an *artificial sound speed*, see [3,51]. The relative error against the phase velocity given by the linear theory of Stokes,  $C_s = \sqrt{gH \frac{\tanh(\kappa H)}{\kappa H}}$ , is depicted in Fig. 1 for  $\kappa H \in [0, 3]$ . The errors obtained for the system in [56] given by (1)–(5) and the hyperbolic Serre–Green–Naghdi model for general bottom topographies proposed in [3] match pretty well, as expected, since both systems are hyperbolic reformulations of the Serre–Green–Naghdi model. The relative errors for the

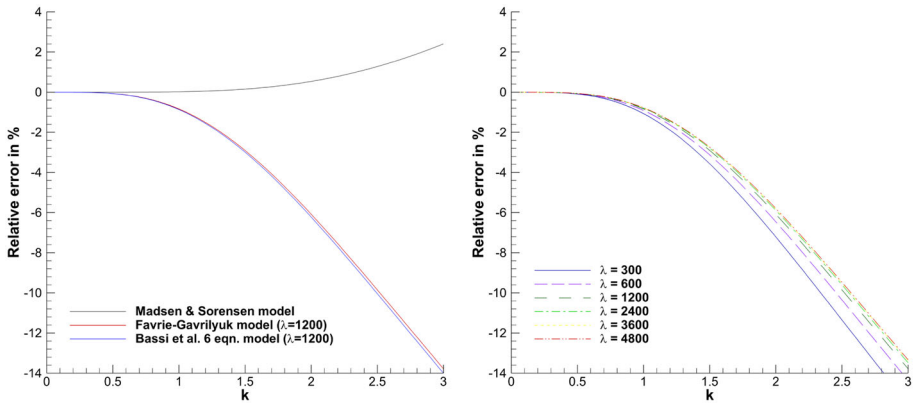


**Fig. 1** Relative error of the phase velocity with respect to the linear theory of Stokes for  $k \in [0, 3]$ . Left: results obtained for  $\lambda = 1200$ ,  $H = 1$ ,  $g = 9.81$ ,  $c^2 = \alpha^2 g H$ : black line: Madsen and Sørensen model (MS), see [76,77]; red line: the Favrie–Gavrilyuk (FG) model [56] studied in this paper; green line: hyperbolic SGN model of Bassi et al. with 6 equations [3]. Right: comparison of the results obtained with the Favrie–Gavrilyuk (FG) model for  $\lambda \in \{300, 600, 1200, 2400, 3600, 4800\}$  (Color figure online)

Madsen and Sørensen model [76,77], which has improved dispersion characteristics, are also included for comparison. Moreover, the right plot in Fig. 1, shows the sensitiveness of the model to variations of  $\lambda$ . We observe that the error decreases when increasing the value of the parameter and the error curves almost overlap for large enough values of  $\lambda$ .

### 2.2 Hyperbolic Reformulation of the Nonlinear Schrödinger Equation

The first order hyperbolic reformulation of the nonlinear Schrödinger equation according to [38] reads

$$\frac{\partial \rho}{\partial t} + \frac{\partial}{\partial x_k} (\rho v_k) = 0, \tag{15}$$

$$\frac{\partial \rho v_i}{\partial t} + \frac{\partial}{\partial x_k} \left( \rho v_i v_k + P \delta_{ik} + \frac{1}{4\rho} p_i p_k \right) = 0, \tag{16}$$

$$\frac{\partial \rho \eta}{\partial t} + \frac{\partial}{\partial x_k} (\rho \eta v_k) = \rho w, \tag{17}$$

$$\frac{\partial \rho w}{\partial t} + \frac{\partial}{\partial x_k} \left( \rho w v_k - \frac{1}{4\rho\beta} p_k \right) = \frac{\lambda}{\beta} \left( 1 - \frac{\eta}{\rho} \right), \tag{18}$$

$$\frac{\partial p_k}{\partial t} + \frac{\partial}{\partial x_k} (p_m v_m - w) + v_m \left( \frac{\partial p_k}{\partial x_m} - \frac{\partial p_m}{\partial x_k} \right) = 0, \tag{19}$$

with the total pressure  $P = \frac{1}{2}\rho^2 - \frac{1}{4\rho} p_m p_m + \lambda \eta \left( 1 - \frac{\eta}{\rho} \right)$  and where  $\lambda \gg 1$  and  $\beta \ll 1$  are two free parameters which make the system (15)–(19) tend to the original hydrodynamic model of the Schrödinger equation in the limit  $\lambda \rightarrow \infty$  and  $\beta \rightarrow 0$ . Please note that compared to [38] the governing equation for  $\mathbf{p}$  is *different* in this paper, since the term  $v_m \left( \frac{\partial p_k}{\partial x_m} - \frac{\partial p_m}{\partial x_k} \right)$  has been added in order to restore the *Galilean invariance* of the system, see [27,47,60,92]. We note that the mathematical structure of system (15) is very similar to the one of (1)–(5), apart from the additional field  $p_k$  that was not present in the hyperbolic reformulation of the

Serre–Green–Naghdi model. We stress that system (15) is endowed with the *curl involution constraint*  $\nabla \times \mathbf{p} = 0$ , which is a direct consequence of (15) if the constraint is satisfied by the initial data. Recall that with  $\mathbf{p} = (p_1, p_2, p_3)^T$  we denote the vector with components  $p_k$ . In [38] the hyperbolicity of (15) was only studied in the one-dimensional case. In this paper we present a complete study in three space dimensions, which yields some interesting findings.

### 2.2.1 Eigenstructure of the Original Weakly Hyperbolic System

The eigenvalues of system (15)–(19) in  $x_1$  direction are

$$\lambda_1 = v_1 - c_\lambda, \quad \lambda_2 = v_1 - c_\beta, \quad \lambda_{3,4,5,6,7} = v_1, \quad \lambda_8 = v_1 + c_\beta, \quad \lambda_9 = v_1 + c_\lambda \quad (20)$$

with the celerities  $c_\lambda = \sqrt{\rho + \frac{1}{4} \frac{p_2^2 + p_3^2}{\rho^2} + \lambda \frac{\eta^2}{\rho^2}}$  and  $c_\beta = \sqrt{\frac{1}{4} \frac{p_2^2 + p_3^2}{\rho^2} + \frac{1}{4\beta\rho^2}}$ . The associated right eigenvectors read

$$\mathbf{r}_{1,9} = \begin{pmatrix} 1 \\ v_1 \mp c_\lambda \\ v_2 \\ v_3 \\ \eta \\ w \\ \frac{p_1}{\rho} \\ 0 \\ 0 \end{pmatrix}, \quad \mathbf{r}_{2,8} = \begin{pmatrix} 0 \\ 0 \\ p_2 \\ p_3 \\ 0 \\ -\beta^{-1} \\ \mp 4\rho c_\beta \\ 0 \\ 0 \end{pmatrix}, \quad \mathbf{r}_3 = \begin{pmatrix} 1 \\ v_1 \\ 0 \\ 0 \\ A \\ B \\ \frac{p_1}{\rho} \\ 0 \\ 0 \end{pmatrix}, \quad \mathbf{r}_4 = \begin{pmatrix} 0 \\ 0 \\ 1 \\ 0 \\ 0 \\ 0 \\ p_2 \\ 0 \\ 0 \end{pmatrix}, \quad \mathbf{r}_5 = \begin{pmatrix} 0 \\ 0 \\ 0 \\ 1 \\ 0 \\ 0 \\ p_3 \\ 0 \\ 0 \end{pmatrix}, \quad (21)$$

with the auxiliary quantities

$$A = \frac{4\lambda\eta\rho - 4\rho^3 - (p_2 + p_3) - 12\lambda\eta^2}{4\lambda(\rho - 2\eta)}, \quad B = w - v_2 p_2 - v_3 p_3.$$

As one can easily see, two eigenvectors are *missing*, hence the system (15)–(19) based on [38] is only *weakly hyperbolic* in the multi-dimensional case. The reason behind this is that the curl involution constraint has not yet been taken into account. In order to fix this issue, in Sect. 2.2.3 we will introduce an *augmented* system that accounts for the curl involution on  $\mathbf{p}$  via a hyperbolic generalized Lagrangian multiplied (GLM) curl cleaning approach, which goes back to the ideas forwarded by Munz et al. [35,83] for divergence-type constraints and in [27,46] for curl-type constraints.

### 2.2.2 Stationary Equilibrium Solution in Cylindrical Coordinates

In this section, we derive a two-dimensional stationary equilibrium solution of system (15)–(19). For this purpose, the equations are first rewritten more conveniently in cylindrical coordinates  $r - \phi - z$ , with the velocity vector written as  $\mathbf{v} = (v_r, v_\phi, v_z)$  and the vector field  $\mathbf{p} = (p_r, p_\phi, p_z)$ . A substantially simplified system in radial direction is obtained by assuming  $\partial_\phi = \partial_z = 0$  and  $v_z = p_z = 0$ . The final system in radial direction reads as follows:

$$\partial_t \rho + \frac{1}{r} \partial_r (r \rho v_r) = 0, \quad (22)$$

$$\partial_t (\rho v_r) + \partial_r \left( \rho v_r^2 + \frac{p_r^2}{4\rho} + P \right) + \frac{\rho(v_r^2 - v_\phi^2)}{r} + \frac{p_r^2 - p_\phi^2}{4\rho r} = 0, \tag{23}$$

$$\partial_t (\rho v_\phi) + \partial_r \left( \rho v_r v_\phi + \frac{p_r p_\phi}{4\rho} \right) + \frac{2}{r} \left( \rho v_r v_\phi + \frac{p_r p_\phi}{4\rho} \right) = 0, \tag{24}$$

$$\partial_t (\rho \eta) + \frac{1}{r} \partial_r (r \rho \eta v_r) = \rho w, \tag{25}$$

$$\partial_t (\rho w) + \frac{1}{r} \partial_r \left( r \rho w v_r - \frac{r}{4\rho\beta} p_r \right) = \frac{\lambda}{\beta} \left( 1 - \frac{\eta}{\rho} \right), \tag{26}$$

$$\partial_t p_r + \partial_r (\mathbf{v} \cdot \mathbf{p} - w) = 0, \tag{27}$$

$$\partial_t p_\phi = 0, \tag{28}$$

where in the last two equations the constraint  $\nabla \times \mathbf{p} = 0$  has been used. We are now looking for a *stationary solution*, hence  $\partial_t = 0$ . We furthermore assume a vortex-type solution with  $v_r = 0$  and  $p_\phi = 0$  so that  $\mathbf{v} \cdot \mathbf{p} = 0$ . With these hypothesis from (25) we obtain  $w = 0$ . The above system (22)–(28) thus reduces to the following ODE system in radial direction:

$$\partial_r \left( \frac{p_r^2}{4\rho} + P \right) - \frac{\rho v_\phi^2}{r} + \frac{p_r^2}{4\rho r} = 0, \tag{29}$$

$$-\frac{1}{r} \partial_r \left( \frac{r}{4\rho\beta} p_r \right) = \frac{\lambda}{\beta} \left( 1 - \frac{\eta}{\rho} \right). \tag{30}$$

We now *prescribe* a radial profile for the density  $\rho$  and for the radial component  $p_r$  as follows:

$$\rho(r) = \rho_0 + \hat{\rho} \operatorname{erf}(L(r - R)), \tag{31}$$

and

$$p_r(r) = p_0 \exp\left(-\frac{1}{2} \frac{(r - R)^2}{\sigma^2}\right). \tag{32}$$

From (30) one then directly obtains the profile  $\eta(r)$  as

$$\eta(r) = \rho(r) \left( 1 + \frac{\beta}{\lambda r} \partial_r \left( \frac{r}{4\rho\beta} p_r(r) \right) \right), \tag{33}$$

while the angular velocity profile  $v_\phi(r)$  is obtained from (29) and reads

$$v_\phi(r) = \sqrt{\frac{p_r^2}{4\rho^2} + \frac{r}{\rho} \partial_r \left( \frac{p_r^2}{4\rho} + P \right)}. \tag{34}$$

The exact expressions for the profiles of  $\eta(r)$  and  $v_\phi(r)$  can be easily obtained via a computer algebra system and are thus not explicitly reported here.

### 2.2.3 Augmented GLM Curl Cleaning System

Following the original ideas of Munz et al. [35,83] concerning hyperbolic divergence cleaning for the Maxwell and MHD equations and their extension to curl involutions in [27,46], we propose the following *augmented system*, where eventual curl errors produced by the numerical scheme are transported away by a Maxwell-type subsystem:

$$\frac{\partial \rho}{\partial t} + \frac{\partial}{\partial x_k} (\rho v_k) = 0, \tag{35}$$



$$\frac{\partial \rho v_i}{\partial t} + \frac{\partial}{\partial x_k} \left( \rho v_i v_k + P \delta_{ik} + \frac{1}{4\rho} p_i p_k \right) = 0, \tag{36}$$

$$\frac{\partial \rho \eta}{\partial t} + \frac{\partial}{\partial x_k} (\rho \eta v_k) = \rho w, \tag{37}$$

$$\frac{\partial \rho w}{\partial t} + \frac{\partial}{\partial x_k} \left( \rho w v_k - \frac{p_k}{4\rho\beta} \right) = \frac{\lambda}{\beta} \left( 1 - \frac{\eta}{\rho} \right), \tag{38}$$

$$\frac{\partial p_k}{\partial t} + \frac{\partial (p_m v_m - w)}{\partial x_k} + v_m \left( \frac{\partial p_k}{\partial x_m} - \frac{\partial p_m}{\partial x_k} \right) + 2\rho a_c \varepsilon_{klm} \frac{\partial \psi_m}{\partial x_l} = 0, \tag{39}$$

$$\frac{\partial \psi_k}{\partial t} + v_m \frac{\partial \psi_k}{\partial x_m} - \frac{a_c}{2\rho} \varepsilon_{klm} \frac{\partial p_m}{\partial x_l} = 0, \tag{40}$$

with the curl cleaning speed  $a_c = const > 0$ . The additional GLM curl cleaning terms have been highlighted in blue, for convenience. From the last two equations we recover the involution constraint  $\nabla \times \mathbf{p} \rightarrow 0$  in the limit  $a_c \rightarrow \infty$ . The equations are also compatible with the energy conservation law (see Appendix B), hence the hyperbolic GLM cleaning proposed in this paper is a *thermodynamically compatible* one, in contrast to the previous hyperbolic GLM cleaning approaches proposed in [27,35,37,46] that were *not* compatible with the conservation of total energy. Note, however, that the GLM divergence cleaning for MHD proposed in [37] was compatible with the conservation of mathematical entropy.

### 2.2.4 Eigenstructure of the Augmented GLM System

The eigenvalues of the thermodynamically compatible augmented GLM curl cleaning system (35)–(40) in  $x_1$  direction are

$$\begin{aligned} \lambda_{1,12} &= v_1 \mp c_\lambda, & \lambda_{2,11} &= v_1 \mp c_\beta, & \lambda_{3,10} &= v_1 \mp a_c, \\ \lambda_{4,9} &= v_1 \mp a_c, & \lambda_{5,6,7,8} &= v_1. \end{aligned} \tag{41}$$

The associated right eigenvectors are

$$\mathbf{r}_{1,12} = \begin{pmatrix} 1 \\ v_1 \mp c_\lambda \\ v_2 \\ v_3 \\ \eta \\ w \\ \frac{p_1}{\rho} \\ 0 \\ 0 \\ 0 \\ 0 \\ 0 \\ 0 \end{pmatrix}, \mathbf{r}_{2,11} = \begin{pmatrix} 0 \\ 0 \\ p_2 \\ p_3 \\ 0 \\ -\beta^{-1} \\ \mp 4\rho c_\beta \\ 0 \\ 0 \\ 0 \\ 0 \\ 0 \end{pmatrix}, \mathbf{r}_5 = \begin{pmatrix} 1 \\ v_1 \\ 0 \\ 0 \\ 0 \\ A \\ B \\ \frac{p_1}{\rho} \\ 0 \\ 0 \\ 0 \\ 0 \\ 0 \end{pmatrix}, \mathbf{r}_6 = \begin{pmatrix} 0 \\ 0 \\ 1 \\ 0 \\ 0 \\ 0 \\ p_2 \\ 0 \\ 0 \\ 0 \\ 0 \\ 0 \\ 0 \end{pmatrix}, \mathbf{r}_7 = \begin{pmatrix} 0 \\ 0 \\ 0 \\ 1 \\ 0 \\ 0 \\ 0 \\ 0 \\ 0 \\ 0 \\ 0 \\ 0 \\ 0 \end{pmatrix}, \tag{42}$$

$$\begin{aligned} \mathbf{r}_8 &= (0, 0, 0, 0, 0, 0, 0, 0, 0, 1, 0, 0)^T, \\ \mathbf{r}_{3,10} &= \left( 0, 0, -\frac{1}{2} p_1 p_3, \frac{1}{2} p_1 p_2, 0, 0, 0, \pm 2 a_c \rho p_3, \mp 2 a_c \rho p_2, 0, a_c p_2, a_c p_3 \right)^T, \\ \mathbf{r}_{4,9} &= (p_3, p_3(v_1 \mp a_c), R_3, R_4, p_3 \eta, R_6, R_7, 0, R_9, 0, R_{11}, 0)^T, \end{aligned} \tag{43}$$

with the auxiliary quantities

$$A = \frac{4\lambda\eta\rho - 4\rho^3 - (p_2 + p_3) - 12\lambda\eta^2}{4\lambda(\rho - 2\eta)}, \quad B = w - v_2p_2 - v_3p_3,$$

$$T = 4\beta a_c^2 \rho^2 - \beta p_2^2 - \beta p_3^2 - 1, \quad \alpha = \rho^3 + \eta^2\lambda,$$

and

$$R_3 = \mp \frac{1}{8} p_3 \frac{\mp 8T a_c \rho^2 v_2 + 4\alpha\beta p_1 p_2 - T p_1 p_2 - p_1 p_2}{\rho^2 a_c T},$$

$$R_4 = \mp \frac{1}{8} \frac{-4T a_c^2 p_1 \rho^2 \mp 8T a_c p_3 \rho^2 v_3 + 4\alpha\beta p_1 p_3^2 + T p_1 p_2^2 + 4T \alpha p_1 - p_1 p_3^2}{\rho^2 a_c T},$$

$$R_6 = \mp \frac{1}{8} p_3 \frac{\mp 8T a_c \rho^2 w + 4c_0^2 p_1 \rho^2 - p_1 p_2^2 - p_1 p_3^2 - 4\alpha p_1}{\rho^2 a_c T},$$

$$R_7 = \frac{1}{2} \frac{p_1 p_3}{\rho T} (4\alpha\beta + T - 1),$$

$$R_9 = \frac{1}{2} \frac{-4a_c^2 \rho^2 + p_2^2 + p_3^2 + 4\alpha}{\rho},$$

$$R_{11} = \mp \frac{1}{4} \frac{-4a_c^2 \rho^2 + p_2^2 + p_3^2 + 4\alpha}{\rho^2}.$$

For  $p_2 \neq 0$  or  $p_3 \neq 0$  the eigenvectors  $\mathbf{r}_{3,10}$  are linearly independent of the others and thus the system is *strongly hyperbolic*. It becomes weakly hyperbolic only for  $p_2 = p_3 = 0$ . One immediately realizes that the eigenvectors  $\mathbf{r}_{1,12}$ ,  $\mathbf{r}_{2,11}$  and  $\mathbf{r}_{5,6,7}$  coincide exactly with those of the original system without GLM curl cleaning.

### 3 Numerical Method

Both dispersive models (1)–(5) and (35)–(40) can be cast into the following general form

$$\frac{\partial \mathbf{Q}}{\partial t} + \nabla \cdot \mathbf{F}(\mathbf{Q}) + \mathbf{B}(\mathbf{Q}) \cdot \nabla \mathbf{Q} = \mathbf{S}(\mathbf{Q}), \tag{44}$$

with the state vector  $\mathbf{Q} \in \Omega_Q \subset \mathbb{R}^m$ , the state space  $\Omega_Q$ , the flux tensor  $\mathbf{F}(\mathbf{Q}) = (\mathbf{f}, \mathbf{g}, \mathbf{h})$ , the nonconservative product  $\mathbf{B}(\mathbf{Q}) \cdot \nabla \mathbf{Q} = \mathbf{B}_1(\mathbf{Q})\partial_x \mathbf{Q} + \mathbf{B}_2(\mathbf{Q})\partial_y \mathbf{Q} + \mathbf{B}_3(\mathbf{Q})\partial_z \mathbf{Q}$  and the algebraic source term  $\mathbf{S}(\mathbf{Q})$ .

For the numerical simulation of the hyperbolic reformulations of the nonlinear dispersive systems introduced in the previous section, and which can all be cast into the general form (44), we employ the family of high order accurate fully-discrete one-step ADER discontinuous Galerkin schemes with *a posteriori* subcell finite volume limiter, see e.g. [17,42,43,49,108]. In the following we provide a brief description of the method. For further details the reader is referred to the above references.

#### 3.1 Fully Discrete One-Step ADER-DG Schemes

The governing PDE systems (1)–(5) and (35)–(40) are discretized on a computational domain  $\Omega$  employing a uniform Cartesian grid with elements  $\Omega_i = [x_i - \frac{\Delta x}{2}, x_i + \frac{\Delta x}{2}] \times [y_i - \frac{\Delta y}{2}, y_i + \frac{\Delta y}{2}]$  with  $\mathbf{x}_i = (x_i, y_i)$  the barycenter of  $\Omega_i$  and  $\Delta x, \Delta y$  the mesh spacing

in  $x$  and  $y$  direction, respectively. Denoting by  $\mathbf{u}_h(\mathbf{x}, t^n)$  the discrete solution of (44) written in the space of piecewise polynomials of degree  $N$ , the discrete solution within  $\Omega_i$  is sought under the form

$$\mathbf{u}_h(\mathbf{x}, t^n) = \phi_l(\mathbf{x}) \hat{\mathbf{u}}_{l,i}^n, \quad \mathbf{x} \in \Omega_i. \tag{45}$$

Here,  $\phi_l(\mathbf{x}) = \varphi_{l_1}(\xi)\varphi_{l_2}(\eta)$  are the basis functions, which are tensor products of one-dimensional basis functions  $\varphi_{l_m}(\chi)$  on the unit interval  $\chi \in \Omega_{\text{ref}} = [0, 1]$ . The mapping from the reference coordinates  $0 \leq \xi, \eta \leq 1$  to the physical coordinates reads  $x = x_i - \frac{1}{2}\Delta x + \xi\Delta x$  and  $y = y_i - \frac{1}{2}\Delta y + \eta\Delta y$ . Here,  $l$  is a multi-index, referring to the one-dimensional basis functions  $\varphi_{l_m}$  to be used in the tensor product. We employ Lagrange interpolation polynomials passing through the Gauss-Legendre quadrature points of a Gaussian quadrature formula with  $N + 1$  nodes. This leads by construction to an *orthogonal* basis. Due to the nodal tensor-product basis, the scheme can be written in a dimension-by-dimension fashion and all operators can be decomposed into products of one-dimensional operators. Multiplication of the governing PDE system (44) by test functions  $\phi_k$ , which are identical to the basis functions, and integration over a space-time control volume  $\Omega_i \times [t^n, t^{n+1}]$  leads to

$$\int_{t^n}^{t^{n+1}} \int_{\Omega_i} \phi_k (\partial_t \mathbf{Q} + \nabla \cdot \mathbf{F}(\mathbf{Q}) + \mathbf{B}(\mathbf{Q}) \cdot \nabla \mathbf{Q}) \, d\mathbf{x} \, dt = \int_{t^n}^{t^{n+1}} \int_{\Omega_i} \phi_k \mathbf{S}(\mathbf{Q}) \, d\mathbf{x} \, dt. \tag{46}$$

Using (45) and integrating the flux divergence term by parts in space and the time derivative by parts in time the above weak problem becomes

$$\begin{aligned} & \left( \int_{\Omega_i} \phi_k \phi_l \, d\mathbf{x} \right) (\hat{\mathbf{u}}_{l,i}^{n+1} - \hat{\mathbf{u}}_{l,i}^n) + \int_{t^n}^{t^{n+1}} \int_{\partial\Omega_i} \phi_k (\mathcal{G}(\mathbf{q}_h^-, \mathbf{q}_h^+) + \mathcal{D}(\mathbf{q}_h^-, \mathbf{q}_h^+)) \cdot \mathbf{n} \, dS \, dt \\ & - \int_{t^n}^{t^{n+1}} \int_{\Omega_i} \nabla \phi_k \cdot \mathbf{F}(\mathbf{q}_h) \, d\mathbf{x} \, dt + \int_{t^n}^{t^{n+1}} \int_{\Omega_i} \phi_k \mathbf{B}(\mathbf{q}_h) \cdot \nabla \mathbf{q}_h \, d\mathbf{x} \, dt = \int_{\Omega_i} \phi_k \mathbf{S}(\mathbf{q}_h) \, d\mathbf{x} \, dt \end{aligned} \tag{47}$$

where  $\mathbf{n}$  is the outward unit normal vector at the cell boundary  $\partial\Omega_i$ , and  $\mathbf{q}_h$  is a local space-time predictor whose computation will be explained in the next section. As usual, in the discontinuous Galerkin finite element method the discrete solution may jump across the cell boundaries, which requires the use of Riemann solvers, see e.g. [98] for a broad overview of exact and approximate Riemann solvers. In this paper, we use either the simple Rusanov-type flux

$$\mathcal{G}(\mathbf{q}_h^-, \mathbf{q}_h^+) \cdot \mathbf{n} = \frac{1}{2} (\mathbf{F}(\mathbf{q}_h^+) + \mathbf{F}(\mathbf{q}_h^-)) \cdot \mathbf{n} - \frac{1}{2} s_{\max} \mathbf{I}_{wb} (\mathbf{q}_h^+ - \mathbf{q}_h^-), \tag{48}$$

with the maximum wavespeed at the interface  $s_{\max} = \max(|\lambda_k(\mathbf{q}_h^-)|, |\lambda_k(\mathbf{q}_h^+)|)$  and the matrix  $\mathbf{I}_{wb} > 0$ . For the hyperbolic reformulation of the Schrödinger equation  $\mathbf{I}_{wb} = \mathbf{I}$  is simply chosen equal to the identity matrix, while for the hyperbolic Serre–Green–Naghdi model (1)–(5)  $\mathbf{I}_{wb}$  needs to be chosen in a special manner in order to make the numerical scheme *well-balanced* for the lake at rest solution [10,59,69], see Sect. 3.3. In alternative, also the more sophisticated generalized Osher-type scheme forwarded in [48] can be used instead of (48). Here,  $\mathbf{q}_h^-$  and  $\mathbf{q}_h^+$  denote the boundary-extrapolated values of the space-time predictor from within the element and its neighbor, respectively. The jump terms in the non conservative products at the boundaries are treated via a path conservative scheme as forwarded by Castro,

Parés and collaborators in [21,22,24,81,86], which are based on the theory of Dal Maso, Le Floch and Murat [78] on nonconservative hyperbolic PDE systems. For a more detailed discussion on the topic, see also [23] and references therein. Path-conservative schemes were generalized to higher order DG schemes for the first time in [43,89]. Based on the path-conservative framework, the construction of so-called well-balanced schemes for shallow water type models is rather straightforward. The jump term in the non-conservative product is computed via a path integral between the two boundary extrapolated values related to the face,  $\mathbf{q}_h^-$  and  $\mathbf{q}_h^+$  as

$$\mathcal{D}(\mathbf{q}_h^-, \mathbf{q}_h^+) \cdot \mathbf{n} = \frac{1}{2} \left( \int_0^1 \mathbf{B}(\boldsymbol{\psi}(\mathbf{q}_h^-, \mathbf{q}_h^+, s)) \cdot \mathbf{n} ds \right) \cdot (\mathbf{q}_h^+ - \mathbf{q}_h^-) \tag{49}$$

where we use the simple straight line segment path

$$\boldsymbol{\psi} = \boldsymbol{\alpha}(\mathbf{q}_h^-, \mathbf{q}_h^+, s) = \mathbf{q}_h^- + s(\mathbf{q}_h^+ - \mathbf{q}_h^-), \quad s \in [0, 1]. \tag{50}$$

In this paper, the path integral (49) is approximated via a simple trapezoidal quadrature rule, which is enough to obtain a well-balanced scheme, as we will see later in Sect. 3.3. In order to achieve an essentially non-oscillatory behaviour at discontinuities and in the regions of strong gradients, the ADER-DG schemes used in this paper are supplemented with an *a posteriori* subcell finite volume limiter, as detailed in [49,108].

### 3.2 Local Space-Time Predictor

The local space-time predictor  $\mathbf{q}_h(\mathbf{x}, t)$  is obtained via a weak formulation of the governing PDE system in space-time, as proposed in [42,44]. This allows to avoid the cumbersome Cauchy-Kovalewskaya procedure used in the original ADER finite volume schemes of Toro et al. [20,96,97,100,101]. The element-local space-time predictor solution is introduced as follows:

$$\mathbf{q}_h(\mathbf{x}, t) = \theta_l(\mathbf{x}, t) \hat{\mathbf{q}}_l, \tag{51}$$

with the space-time basis functions  $\theta_l = \theta_l(\mathbf{x}, t) = \varphi_{l_0}(\tau)\varphi_{l_1}(\xi)\varphi_{l_2}(\eta)$ , which are tensor products of the spatial basis functions already introduced before and an additional nodal basis function for the time dependency, and with  $t = t^n + \tau\Delta t$ . Multiplying (44) by a space-time test function  $\theta_k$  and integrating over  $\Omega_i \times [t^n, t^{n+1}]$ , one obtains

$$\begin{aligned} & \int_{t^n}^{t^{n+1}} \int_{\Omega_i} \theta_k \partial_t \mathbf{q}_h \, d\mathbf{x} \, dt + \int_{t^n}^{t^{n+1}} \int_{\Omega_i} \theta_k \nabla \cdot \mathbf{F}(\mathbf{q}_h) \, d\mathbf{x} \, dt \\ & + \int_{t^n}^{t^{n+1}} \int_{\Omega_i^\circ} \theta_k \mathbf{B}(\mathbf{q}_h) \cdot \nabla \mathbf{q}_h \, d\mathbf{x} \, dt = \int_{\Omega_i} \theta_k \mathbf{S}(\mathbf{q}_h) \, d\mathbf{x} \, dt. \end{aligned} \tag{52}$$

Integration by parts of the first term in time yields

$$\int_{\Omega_i} \theta_k(\mathbf{x}, t^{n+1}) \mathbf{q}_h(\mathbf{x}, t^{n+1}) \, d\mathbf{x} - \int_{\Omega_i} \theta_k(\mathbf{x}, t^n) \mathbf{u}_h(\mathbf{x}, t^n) \, d\mathbf{x} - \int_{t^n}^{t^{n+1}} \int_{\Omega_i} \partial_t \theta_k \mathbf{q}_h \, d\mathbf{x} \, dt$$

$$+ \int_{t^n}^{t^{n+1}} \int_{\Omega_i} \theta_k \nabla \cdot \mathbf{F}(\mathbf{q}_h) \, d\mathbf{x} \, dt + \int_{t^n}^{t^{n+1}} \int_{\Omega_i^\circ} \theta_k \mathbf{B}(\mathbf{q}_h) \cdot \nabla \mathbf{q}_h \, d\mathbf{x} \, dt = \int_{\Omega_i} \theta_k \mathbf{S}(\mathbf{q}_h) \, d\mathbf{x} \, dt, \tag{53}$$

which is an element-local system for the unknown degrees of freedom  $\hat{\mathbf{q}}_k$  of the space-time predictor  $\mathbf{q}_h(\mathbf{x}, t)$  and which can be computed in terms of the known spatial degrees of freedom  $\hat{\mathbf{u}}_{l,i}^n$  of the discrete solution  $\mathbf{u}_h(\mathbf{x}, t^n)$ . The solution of (53) can be found via a fast-converging iterative fixed point scheme, the convergence of which was proven in [17]. As any explicit numerical method for hyperbolic systems, our scheme is subject to a usual CFL-type time step restriction, requiring

$$\Delta t \leq \frac{C}{2N + 1} \frac{\Delta x}{\max_{k,l,i} |\lambda_k(\hat{\mathbf{u}}_{l,i}^n)|} \tag{54}$$

with  $C < 1$ , see [42], and where the maximum is taken over all cells and degrees of freedom in the computational domain. It is clear that (54) contains the parameter  $\lambda$ , but the time step scales only *linearly* in  $\Delta x$  and not cubically. Furthermore, the proposed explicit DG scheme does not require the solution of big linear systems, unlike the fully implicit space-time DG scheme for dispersive systems proposed in [45].

### 3.3 Well-Balanced Property for the Favrie–Gavrilyuk Model with Variable Bottom Topography

In this section we prove the well-balanced property [69,104] of the first order version of our ADER-DG schemes in one space-dimension, i.e. for  $N = 0$  and  $d = 1$ , which remains the key ingredient of the well-balancing also for higher order schemes since it involves the numerical flux and the jump terms. For high order well-balanced reconstructions see [21,22,57,58]. Later in this section, we also study the well-balanced behavior of the actual implementation of the numerical scheme.

For  $N = 0$  we have only one single test and basis function  $\phi_1 = \theta_1 = 1$  and one single degree of freedom in space and time  $\hat{\mathbf{q}}_{1,i}^n = \hat{\mathbf{u}}_{1,i}^n = \mathbf{Q}_i^n$  per cell, which corresponds to the usual cell average  $\mathbf{Q}_i^n$ . The scheme (47) then reduces to the following path-conservative finite volume method:

$$\begin{aligned} \mathbf{Q}_i^{n+1} &= \mathbf{Q}_i^n - \frac{\Delta t}{\Delta x} (\mathcal{G}(\mathbf{Q}_i^n, \mathbf{Q}_{i+1}^n) - \mathcal{G}(\mathbf{Q}_{i-1}^n, \mathbf{Q}_i^n)) \\ &\quad - \frac{\Delta t}{\Delta x} (\mathcal{D}(\mathbf{Q}_i^n, \mathbf{Q}_{i+1}^n) + \mathcal{D}(\mathbf{Q}_{i-1}^n, \mathbf{Q}_i^n)) + \Delta t \mathbf{S}(\mathbf{Q}_i^n), \end{aligned} \tag{55}$$

with the numerical flux and the path-conservative jump term that in one space dimension ( $d = 1$ ) reduce to

$$\mathcal{G}(\mathbf{q}_h^-, \mathbf{q}_h^+) = \frac{1}{2} (\mathbf{f}(\mathbf{q}_h^+) + \mathbf{f}(\mathbf{q}_h^-)) - \frac{1}{2} s_{\max} \mathbf{I}_{wb} (\mathbf{q}_h^+ - \mathbf{q}_h^-), \tag{56}$$

and

$$\mathcal{D}(\mathbf{q}_h^-, \mathbf{q}_h^+) = \frac{1}{2} \left( \frac{1}{2} \mathbf{B}_1(\mathbf{q}_h^-) + \frac{1}{2} \mathbf{B}_1(\mathbf{q}_h^+) \right) \cdot (\mathbf{q}_h^+ - \mathbf{q}_h^-). \tag{57}$$

Recall that the non-hydrostatic pressure is given by  $p = \frac{\lambda}{3} \frac{\eta}{h} (1 - \frac{\eta}{h})$  and that

$$\mathbf{f}(\mathbf{Q}) = \begin{pmatrix} hv_1 \\ hv_1^2 + hp \\ hv_1v_2 \\ hv_1\eta \\ hv_1w \\ 0 \end{pmatrix}, \quad \mathbf{B}_1(\mathbf{Q}) = \begin{pmatrix} 0 & 0 & 0 & 0 & 0 & 0 \\ gh & 0 & 0 & 0 & 0 & gh + \frac{3}{2} \frac{h}{\eta} p \\ 0 & 0 & 0 & 0 & 0 & 0 \\ 0 & 0 & 0 & 0 & 0 & \frac{3}{2} hv_1 \\ 0 & 0 & 0 & 0 & 0 & 0 \\ 0 & 0 & 0 & 0 & 0 & 0 \end{pmatrix}. \tag{58}$$

For the system (1)–(5) the following well-balanced identity matrix has been chosen throughout this paper:

$$\mathbf{I}_{wb} = \begin{pmatrix} 1 & 0 & 0 & 0 & 0 & 1 \\ 0 & 1 & 0 & 0 & 0 & 0 \\ 0 & 0 & 1 & 0 & 0 & 0 \\ 0 & 0 & 0 & 1 & 0 & \tilde{h} \\ 0 & 0 & 0 & 0 & 1 & 0 \\ 0 & 0 & 0 & 0 & 0 & 0 \end{pmatrix}, \quad \text{with} \quad \tilde{h} = h^- + h^+. \tag{59}$$

Lake at rest solutions for system (1)–(5) are characterized by

$$\zeta = h + b = \text{const.}, \quad v_1 = v_2 = 0, \quad \eta = h, \quad w = 0, \tag{60}$$

and are stationary solutions of (1)–(5) for arbitrary bottom  $b$ . We now *prove* that the scheme (55) maintains solutions of the type (60) *exactly* at the discrete level for all times. Since  $\eta = h$  and  $w = 0$ , it is obvious that the discrete source term  $\mathbf{S}(\mathbf{Q}_i^n)$  vanishes. We now analyze the numerical flux  $\mathcal{G}(\mathbf{Q}_i^n, \mathbf{Q}_{i+1}^n)$  and the path-conservative jump term  $\mathcal{D}(\mathbf{Q}_i^n, \mathbf{Q}_{i+1}^n)$ . For  $\zeta = \text{const.}$  and  $\eta = h$  we have  $p = 0$  and the following relations for the jumps in  $h$ ,  $\eta$  and  $b$ :

$$\Delta\zeta = \zeta^+ - \zeta^- = \Delta h + \Delta b = 0, \quad \Delta h = h^+ - h^-, \quad \Delta b = b^+ - b^-, \tag{61}$$

$$\Delta h = -\Delta b, \quad \Delta \eta = \Delta h. \tag{62}$$

From these relations and  $\eta = h$  we can compute the jump in the conservative variable  $h\eta$  as

$$\Delta(h\eta) = h^+\eta^+ - h^-\eta^- = \eta^- \Delta h + h^- \Delta \eta + \Delta h \Delta \eta = -2h^- \Delta b + \Delta b^2. \tag{63}$$

We thus obtain for the jump in the state vector

$$\mathbf{q}_h^+ - \mathbf{q}_h^- = \begin{pmatrix} -\Delta b \\ 0 \\ 0 \\ -2h^- \Delta b + \Delta b^2 \\ 0 \\ \Delta b \end{pmatrix} \tag{64}$$

and with  $p^- = p^+ = 0$  and  $v_1^- = v_1^+ = 0$  the path integral of  $\mathbf{B}_1$  becomes

$$\frac{1}{2} \mathbf{B}_1(\mathbf{q}_h^-) + \frac{1}{2} \mathbf{B}_1(\mathbf{q}_h^+) = \begin{pmatrix} 0 & 0 & 0 & 0 & 0 & 0 \\ g \frac{1}{2} (h^- + h^+) & 0 & 0 & 0 & 0 & g \frac{1}{2} (h^- + h^+) \\ 0 & 0 & 0 & 0 & 0 & 0 \\ 0 & 0 & 0 & 0 & 0 & 0 \\ 0 & 0 & 0 & 0 & 0 & 0 \\ 0 & 0 & 0 & 0 & 0 & 0 \end{pmatrix}. \tag{65}$$

**Table 1** Numerical verification of the well-balanced property for a first order DG scheme,  $N = 0$ , applied to the hyperbolic reformulation of the SGN model (1)–(5). The reported errors refer to the  $L^\infty$  errors for the variables  $h, v_1, \eta$  and  $w$  at a final time of  $t = 2$

Machine precision	$L^\infty(h)$	$L^\infty(v_1)$	$L^\infty(\eta)$	$L^\infty(w)$
Single precision	$5.3644 \times 10^{-7}$	$7.6682 \times 10^{-6}$	$4.7684 \times 10^{-7}$	$1.6719 \times 10^{-5}$
Double precision	$1.5543 \times 10^{-15}$	$3.9948 \times 10^{-14}$	$1.2212 \times 10^{-15}$	$9.0634 \times 10^{-14}$
Quadruple precision	$6.7408 \times 10^{-34}$	$2.4366 \times 10^{-32}$	$4.8148 \times 10^{-34}$	$3.7267 \times 10^{-32}$

From (65) and (64) it follows that

$$\mathcal{D}(\mathbf{q}_h^-, \mathbf{q}_h^+) \cdot \mathbf{n} = \frac{1}{2} \left( \frac{1}{2} \mathbf{B}_1(\mathbf{q}_h^-) + \frac{1}{2} \mathbf{B}_1(\mathbf{q}_h^+) \right) \cdot (\mathbf{q}_h^+ - \mathbf{q}_h^-) = 0, \tag{66}$$

hence the path-conservative jump term vanishes. Next, we analyze the numerical flux (56). Since  $v_1^- = v_1^+ = 0$  and  $p^- = p^+ = 0$  it follows immediately that  $\mathbf{f}(\mathbf{q}_h^-) = \mathbf{f}(\mathbf{q}_h^+) = 0$ . The last term to analyze is the numerical viscosity, for which we obtain

$$\mathbf{I}_{wb} \cdot (\mathbf{q}_h^+ - \mathbf{q}_h^-) = \begin{pmatrix} 1 & 0 & 0 & 0 & 0 & 1 \\ 0 & 1 & 0 & 0 & 0 & 0 \\ 0 & 0 & 1 & 0 & 0 & 0 \\ 0 & 0 & 0 & 1 & 0 & \tilde{h} \\ 0 & 0 & 0 & 0 & 1 & 0 \\ 0 & 0 & 0 & 0 & 0 & 0 \end{pmatrix} \cdot \begin{pmatrix} -\Delta b \\ 0 \\ 0 \\ -2h^- \Delta b + \Delta b^2 \\ 0 \\ \Delta b \end{pmatrix} = 0, \tag{67}$$

since  $\tilde{h} = h^- + h^+ = 2h^- - \Delta b$  and thus  $-2h^- \Delta b + \Delta b^2 + \tilde{h} \Delta b = 0$ . Therefore, also the numerical flux  $\mathcal{G}(\mathbf{q}_h^-, \mathbf{q}_h^+) = 0$  vanishes at each element interface. Hence, for lake at rest solutions (60) the scheme (55) reduces to

$$\mathbf{Q}_i^{n+1} = \mathbf{Q}_i^n, \tag{68}$$

i.e. lake at rest solutions are exactly preserved at the discrete level, or, in other words, the scheme is well-balanced.

To verify the well-balanced property also numerically, we carry out the following simple test. In a 1D domain  $\Omega = [-5, +5]$  we define the following initial condition, with  $H(x)$  being the Heaviside function:

$$\zeta = 1, \quad b = \frac{1}{2} \exp\left(-\frac{1}{2} \frac{(x + 2.5)^2}{0.5^2}\right) + \frac{1}{2} H(x - 2.5), \tag{69}$$

$$h = \zeta - b, \quad \eta = h, \quad v_1 = v_2 = w = 0, \tag{70}$$

which is a lake at rest solution (60) of system (1)–(5). The domain  $\Omega$  is discretized by 200 equidistant control volumes and simulations are run with the first order scheme (55) using (56) with (59) and (57) until a final time of  $t = 2$  using a CFL number of CFL= 0.5 and setting  $\lambda = 1200$ . We report the  $L^\infty$  errors for the variables  $h, v_1, \eta$  and  $w$  at time  $t = 2$  in Table 1 using single, double and quadruple precision. The computational results clearly show that the method is well-balanced up to machine precision, as expected.

## 4 Numerical Results

### 4.1 Hyperbolic Reformulation of the Serre–Green–Naghdi Model

#### 4.1.1 Numerical Convergence Study

In this section, we simulate the propagation of a solitary wave over a flat bottom in the computational domain  $\Omega = [-50, +50] \times [0, +25]$  with final simulation time  $t = 2$ . Periodic boundary conditions have been imposed everywhere. The amplitude of the soliton is  $A = 0.1$ , the still water depth is  $H = 1$  and initially the soliton is centered in  $x = 0$ . For all simulations of this section  $\lambda = 6000$  has been chosen. Since the exact solution for a solitary wave of the original SGN model, see e.g. [56], is *not* an exact solution of the hyperbolic model (1)–(5) we proceed as suggested in [3], i.e. by finding a travelling wave solution in  $x$  direction for the hyperbolic model (1)–(5) of the form

$$\mathbf{Q}(x, t) = \mathbf{Q}(\xi), \quad \text{with} \quad \xi = x - Vt, \tag{71}$$

where  $V = \sqrt{g(H + A)}$  is the velocity of the soliton and the similarity variable is denoted by  $\xi$ . Under these assumptions we get  $\partial_t \mathbf{Q} = -V \mathbf{Q}'$  and  $\partial_x \mathbf{Q} = \mathbf{Q}'$ . Hence, the PDE system (44) can be rewritten as

$$-V \mathbf{Q}' + \mathbf{A}(\mathbf{Q})\mathbf{Q}' = \mathbf{S}(\mathbf{Q}) \tag{72}$$

with the matrix  $\mathbf{A}(\mathbf{Q}) = \partial \mathbf{f} / \partial \mathbf{Q} + \mathbf{B}_1(\mathbf{Q})$  containing the flux Jacobian and the non-conservative product. For flat bottom, as considered here, the latter does not contribute. The PDE system (44) finally reduces to the following nonlinear ODE system

$$\mathbf{Q}' = (\mathbf{A}(\mathbf{Q}) - V \mathbf{I})^{-1} \mathbf{S}(\mathbf{Q}), \tag{73}$$

with initial condition  $\mathbf{Q}(\xi_0) = (H, 0, 0, H - \varepsilon, 0, 0)$  and with  $\mathbf{I}$  the identity matrix. For our numerical tests we set  $g = 9.81$ ,  $H = 1$ ,  $A = 0.1$  and the perturbation  $\varepsilon = 10^{-10}$ . The ODE system (73) is solved with a 6<sup>th</sup> order DG scheme in time, see [41], in order to provide a highly accurate initial condition for the solitary wave of the hyperbolic SGN system (1)–(5).

We now simulate the propagation of the solitary wave until  $t = 2$  using ADER-DG schemes of polynomial approximation degrees  $N = 2, 3, 4, 5$  on a sequence of successively refined meshes. The  $L^2$  errors and corresponding numerical convergence rates are shown in Table 2. Overall we find the expected convergence order  $N + 1$  of our high order ADER-DG schemes.

In order to investigate the dependence of the solutions of the model (1)–(5) on the parameter  $\lambda$  more thoroughly, we use the high order ODE solver [41] in order to calculate the shape of a solitary wave moving with velocity  $V = 4$  in still water of depth  $H_0 = 1$  as a function of  $\lambda \in [75, 6000]$ , i.e. with  $\lambda$  varying over about two orders of magnitude. The dependence of the shape of the resulting solitary waves on  $\lambda$  is depicted in Fig. 2. One can observe that the shapes for  $\lambda = 1200$  and  $\lambda = 6000$  match very well. For this reason, if not stated otherwise, in the following numerical experiments we will set  $\lambda = 1200$ , since  $\lambda = 6000$  does not give visible improvements for practical simulations, but due to the CFL condition reduces the time step by more than a factor of 2 compared to the choice  $\lambda = 1200$ .

To give an idea of the computational cost of the approach presented in this paper, we compare it with the cost of a fully implicit space-time DG scheme [45] applied to the dispersive system of Madsen and Sørensen [76] with third order derivatives. The computational setup is the following: we consider the 1D domain  $\Omega = [-20, +20]$  with periodic boundary



**Table 2** Numerical convergence results for high order ADER-DG schemes of polynomial approximation degree  $N \in \{2, 3, 4, 5\}$  for the hyperbolic reformulation of the Serre–Green–Naghdi model (1)–(5) according to [56]. A uniform Cartesian mesh composed of  $N_x \times 4$  elements has been used. The  $L^2$  error norms and corresponding orders of convergence (in bold) refer to the variables  $v_1$ ,  $\eta$  and  $w$  at a final time of  $t = 2$

$N_x$	$L^2(v_1)$	$\mathcal{O}(v_1)$	$L^2(\eta)$	$\mathcal{O}(\eta)$	$L^2(w)$	$\mathcal{O}(w)$
<i>ADER-DG N = 2</i>						
64	3.6522E-02		3.0976E-02		1.0777E-01	
128	3.2086E-03	<b>3.5</b>	5.5742E-03	<b>2.5</b>	1.9539E-02	<b>2.5</b>
256	3.3057E-04	<b>3.3</b>	9.9164E-04	<b>2.5</b>	3.5658E-03	<b>2.5</b>
512	3.9409E-05	<b>3.1</b>	1.6786E-04	<b>2.6</b>	6.5569E-04	<b>2.4</b>
<i>ADER-DG N = 3</i>						
32	3.2963E-02		1.8827E-02		7.3790E-02	
64	2.2957E-03	<b>3.8</b>	2.8810E-03	<b>2.7</b>	8.1905E-03	<b>3.2</b>
128	1.8157E-04	<b>3.7</b>	2.6749E-04	<b>3.4</b>	1.2853E-03	<b>2.7</b>
256	4.9323E-06	<b>5.2</b>	1.3652E-05	<b>4.3</b>	7.3061E-05	<b>4.1</b>
<i>ADER-DG N = 4</i>						
16	3.3731E-01		1.9062E-01		5.1416E-01	
32	4.6940E-03	<b>6.2</b>	4.3726E-03	<b>5.4</b>	1.4092E-02	<b>5.2</b>
64	3.4619E-04	<b>3.8</b>	4.0245E-04	<b>3.4</b>	2.2843E-03	<b>2.6</b>
128	7.0624E-06	<b>5.6</b>	1.3174E-05	<b>4.9</b>	7.4341E-05	<b>4.9</b>
<i>ADER-DG N = 5</i>						
16	3.9790E-02		1.8485E-02		8.1569E-02	
32	1.2395E-03	<b>5.0</b>	1.0505E-03	<b>4.1</b>	5.4111E-03	<b>3.9</b>
64	2.0243E-05	<b>5.9</b>	3.1764E-05	<b>5.0</b>	1.3082E-04	<b>5.4</b>
128	3.1760E-07	<b>6.0</b>	6.0393E-07	<b>5.7</b>	2.4188E-06	<b>5.8</b>

conditions in which a solitary wave with  $H_0 = 1$  and  $V = 4$  is moving, see also Fig. 2 for a graphical representation of the shape of the wave. At time  $t = 10$  the exact solution of the problem is given again by the initial condition. We apply the explicit ADER-DG scheme to the hyperbolic model (1)–(5) with  $\lambda = 1200$  and the implicit space-time DG scheme [45] to the Madsen and Sørensen model [76], which contains higher order derivatives. In both cases solitary waves with the same parameters are considered ( $H_0 = 1, V = 4$ ). Both schemes are nominally fourth order accurate, i.e. with polynomial approximation degree  $N = 3$  and the computational mesh used in both simulations is composed of  $N_x = 200$  elements. In Table 3 we report the obtained  $L^2$  error norms for  $h$  and  $h v_1$  at time  $t = 10$  for both schemes, as well as the necessary CPU time and the time per degree of freedom update (TDU). The TDU metric is computed as  $TDU = WCT / (N_t N_x (N + 1))$ , where WCT is the total wall clock time needed for the simulation,  $N_x$  is the number of elements in space,  $N + 1$  is the number of degrees of freedom per element and  $N_t$  is the total number of timesteps needed to reach the final time. Both simulations were run in serial on one single CPU core of an Intel i9-7900X workstation with 32 GB of RAM. From the results shown in Table 3 one can see that both methods reach comparable errors in the variable  $h v_1$ , but the explicit ADER-DG scheme applied to the hyperbolic model (1)–(5) is about three times faster compared to the fully implicit space-time DG scheme applied to the dispersive model [76]. The cost per single degree of freedom update (TDU) is three orders of magnitude larger for the fully-implicit

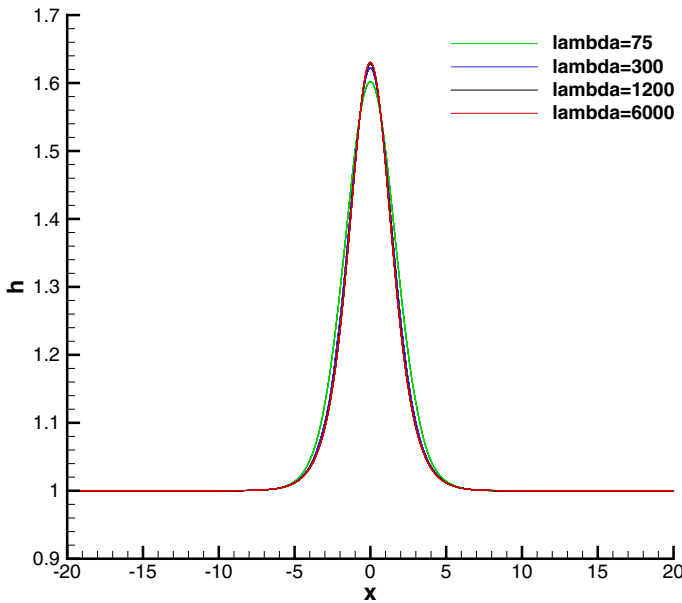


**Fig. 2** Shape of a solitary wave of the model (1)–(5) moving with velocity  $V = 4$  in still water of depth  $H_0 = 1$  as a function of the parameter  $\lambda$

**Table 3** Comparison of errors and CPU times for the propagation of a solitary wave with  $H_0 = 1$  and  $V = 4$  at time  $t = 10$  using the explicit ADER-DG scheme applied to the hyperbolic system (1)–(5) with the fully implicit space-time DG scheme described in [45] applied to the Madsen and Sørensen model [76]. We also report the time needed to update a single degree of freedom for one time step (TDU)

Method	$L^2(h)$	$L^2(hv_1)$	CPU time [s]	TDU [s]
Explicit ADER-DG	$1.6703 \times 10^{-6}$	$3.7603 \times 10^{-6}$	125.7	$1.1 \times 10^{-6}$
Implicit STDG	$1.7189 \times 10^{-7}$	$2.0561 \times 10^{-6}$	476.9	$3.7 \times 10^{-3}$

space-time DG scheme. We expect that in multiple space dimensions and in the context of a parallel implementation on distributed memory machines, the comparison may be even more in favor of the explicit scheme applied to the hyperbolic reformulation of the dispersive system.

### 4.1.2 Solitary Wave

As second part of the previous test, we now analyse the propagation of a solitary wave of the *original* Serre–Green–Naghdi system over a flat bottom for a longer simulation time  $t = 100/\sqrt{g(H + A)}$ . The exact solution of a solitary wave for the original Serre–Green–Naghdi equation reads

$$h(\xi) = H + A \operatorname{sech}^2 \left( \frac{\xi}{2} \sqrt{\frac{3A}{H^2(H + A)}} \right), \tag{74}$$

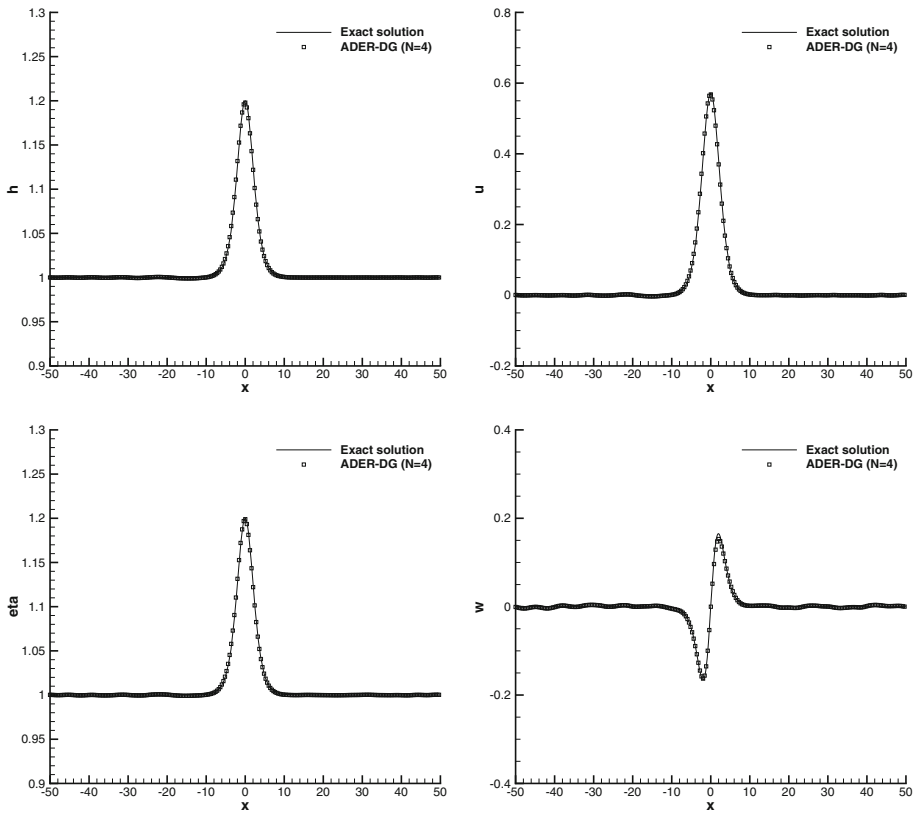


**Fig. 3** Exact (solid line) and numerical solution (squares) for the solitary wave at time  $t = 100/\sqrt{g(H + A)}$ . Water depth  $h$  (top left), velocity component  $v_1$  (top right),  $\eta$  (bottom left) and  $w$  (bottom right)

$$v_1(\xi) = V \left( 1 - \frac{H}{h(\xi)} \right), \tag{75}$$

with  $\xi = x - Vt$  and  $V = \sqrt{g(H + A)}$ , see e.g. [56]. As suggested in [38], the remaining variables of the system are set as

$$\eta(\xi) = h(\xi), \quad w = -h\partial_x v_1, \quad v_2 = 0, \quad b = 0, \tag{76}$$

i.e. with  $\eta = h$  the system is initialized so that  $p = 0$ . For this test we set  $H = 1$ ,  $A = 0.2$  and  $\lambda = 1200$ . The domain is again  $\Omega = [-50, +50] \times [0, +25]$  and periodic boundary conditions are defined everywhere. The results obtained with an ADER-DG scheme of polynomial approximation degree  $N = 4$  on a uniform Cartesian mesh composed of  $1080 \times 4$  elements after one complete revolution of the soliton are depicted in Fig. 3 and are compared against the exact solution given by (74)–(76). As expected, the shape of the soliton has been well preserved, showing only some small spurious oscillations away from the soliton.

### 4.1.3 Solitary Wave Over a Step

The solitary wave over a step benchmark proposed in [93] and also used in [3,4] is employed as a first test with nontrivial bottom topography aiming to compare the numerical results obtained

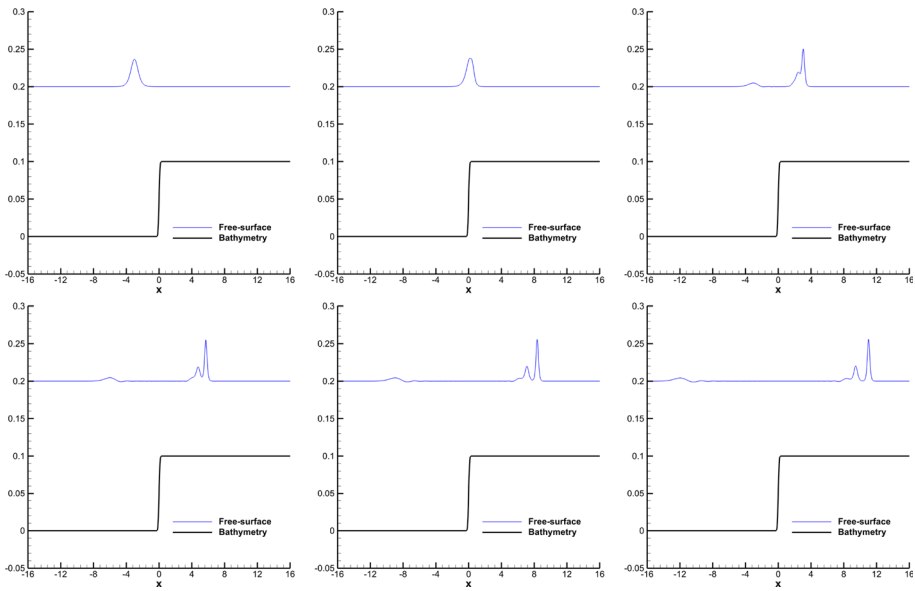


**Fig. 4** 1D cut along  $y = 0$  of the free surface (blue line) and the bottom bathymetry (black line) at times  $t \in \{0, 2.148, 4.296, 6.444, 8.592, 10.74\}$  (from left top to right bottom) for the solitary wave over a step test case (Color figure online)

with experimental data. We consider the computational domain  $\Omega = [-16, +16] \times [-1, +1]$  and a bathymetry characterized by a step shaped obstacle of height  $H_{\text{obs}} = 0.1$  positioned at  $x_{\text{obs}} = 0$ . The obstacle has been smoothed employing the error function

$$z_b = 0.05 (\text{erf}(8x) + 1). \tag{77}$$

The still water depth is  $H = 0.2$  and  $\lambda = 1200$  is chosen. A soliton of amplitude  $A = 0.0365$  is initially located at  $x_{\text{sol}} = -3$ . To generate the initial conditions for the different variables the corresponding ODE system (73) is solved using a 10<sup>th</sup> order DG scheme in time. Periodic boundary conditions are defined in  $y$  direction while on the left and right boundaries we set the initial data as Dirichlet boundary conditions.

The domain is discretized with 2000 elements in the horizontal direction and the simulation is run with polynomial degree  $N = 3$ . A 1D cut of the free surface obtained at times  $t \in \{0, 2.148, 4.296, 6.444, 8.592, 10.74\}$  is depicted in Fig. 4. As expected, the soliton initially propagates smoothly growing when approaching the bottom step. Then, it splits into two transmitted waves in forward direction. A secondary reflecting wave, followed by a train of small dispersive waves, is generated and propagated in the opposite direction to the incoming soliton. The use of the *a posteriori* FV limiter results in the damping of the small spurious oscillations appearing in correspondence to the obstacle that could be seen for the hyperbolic dispersive models used in [3,4]. Figure 5 reports the time evolution of the ratio between the wave amplitude and the still water depth,  $\frac{A}{H} = \frac{h+b-H}{H}$ , at the fixed observation points  $x \in \{-9, -3, 0, 3, 6, 9\}$ . The numerical solution of the model (1)–(5) obtained in this paper agrees well with the results obtained using the alternative hyperbolic reformulations of the SGN model employed in [3,4,51]. Moreover, we also observe a good agreement with experimental data.

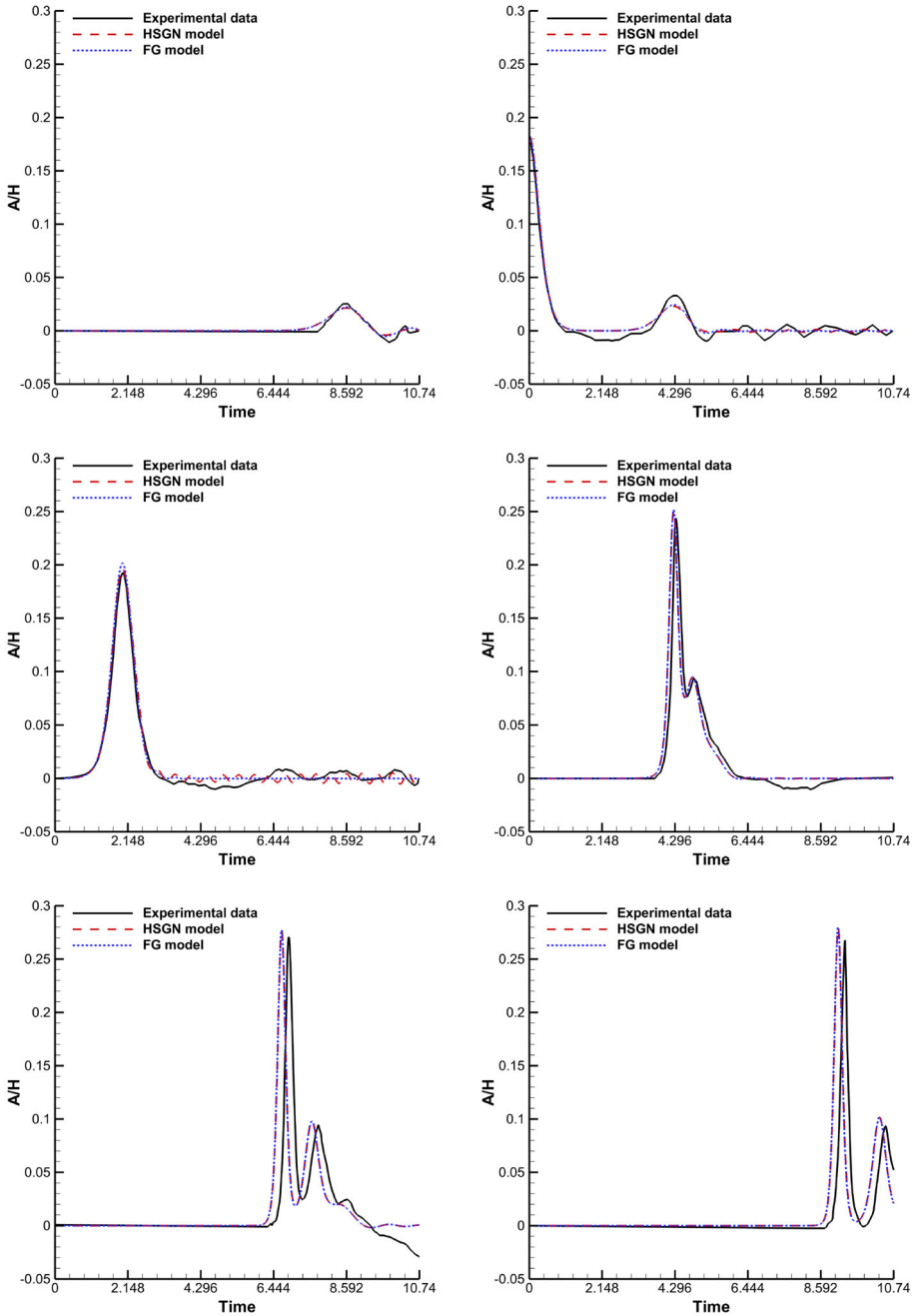


**Fig. 5** Comparison of the time evolution of numerical results obtained for the soliton over a step test case using the ADER-DG  $N = 3$  scheme for the Favrie–Gavrilyuk (FG) model (blue dotted line) against the solution obtained with the hyperbolic SGN model for mild bottom bathymetry (red dashed line), [3,51,56], and the experimental data given in [93] (black line) at locations  $x \in \{-9, -3, 0, 3, 6, 9\}$  (from left top to right bottom) (Color figure online)

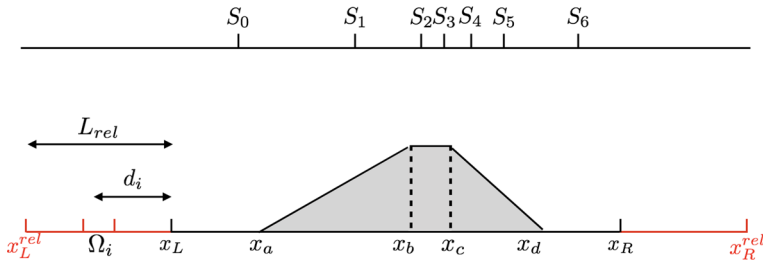


**Fig. 6** Computational domain and locations of the wave gauges for the periodic waves over a submerged bar test case. Computational domain:  $\Omega = [-10, +40]$ . Relaxation zones:  $\Omega_L^{rel} = [-20, -10]$ ,  $\Omega_R^{rel} = [+40, +50]$ . Submerged bar:  $x_a = 6$ ,  $x_b = 12$ ,  $x_c = 14$ ,  $x_d = 17$ . Locations of the wave gauges:  $S_0 = 6.0$ ,  $S_1 = 10.8$ ,  $S_2 = 12.8$ ,  $S_3 = 13.8$ ,  $S_4 = 14.8$ ,  $S_5 = 16.0$ ,  $S_6 = 17.6$

### 4.1.4 Periodic Waves Over a Submerged Bar

We now study the results obtained for the periodic waves over a submerged bar benchmark presented in [7,8,72]. The computational domain is depicted in Fig. 6. The physical domain is enlarged in  $x$ -direction to introduce damping zones of length  $L_{rel} = 10$  allowing to define a wavemaker and an absorbing boundary condition guaranteeing a smooth transition between the target solution  $\mathbf{u}^*$  and the solution  $\mathbf{u}_h$  inside the computational domain. To define the periodic signal at the left boundary a sinusoidal function is employed,

$$\begin{aligned}
 h^*(t) &= H + A_\infty \sin(\omega t), & v_1^*(t) &= A_\infty \sin(\omega t) \sqrt{g(H + A_\infty)}, \\
 v_2^*(t) &= 0, & \eta^*(t) &= h^*(t), & w^*(t) &= 0,
 \end{aligned}
 \tag{78}$$

where the amplitude,  $A_\infty$ , is selected to match the initial amplitude of the periodic waves given by the experimental data at the wave gauge  $S_0 = 0$  and  $\omega = 2\pi/T$  is the angular frequency,  $T$  the wave period, also fixed attending to the experimental data. Regarding the absorbing boundary condition we define, as target solution,

$$h^*(t) = \eta^*(t) = H, \quad u^*(t) = w^*(t) = 0,
 \tag{79}$$

preventing wave reflection. Inside the relaxation zones the solution in an element  $\Omega_i$  is computed as

$$\tilde{\mathbf{u}}_h = m_i \mathbf{u}_h + (1 - m_i) \mathbf{u}^*
 \tag{80}$$

with

$$m_i = \sqrt{1 - \left(\frac{d_i}{L_{rel}}\right)^2},
 \tag{81}$$

$d_i$  the distance between the barycentre of  $\Omega_i$  and the corresponding boundary,  $x_L$  or  $x_R$ . Periodic boundary conditions are defined in  $y$  direction.

The experimental data available corresponds to two different settings. The first of them, a low frequency test (LF), is characterized by  $A_\infty = 0.01$ ,  $T = 2.0205$ . Meanwhile, for the high frequency case (HF) we have  $A_\infty = 1.286E - 2$ ,  $T = 1.2624$ . The polynomial degree in both simulations is  $N = 3$ . The *a posteriori* subcell finite volume limiter is employed to prevent spurious oscillations, see [17,49,108]. The parameter  $\lambda$  is chosen as  $\lambda = 1200$ .

To analyse the results obtained, we consider six wave gauges located in  $S_1 = 10.8$ ,  $S_2 = 12.8$ ,  $S_3 = 13.8$ ,  $S_4 = 14.8$ ,  $S_5 = 16.0$ ,  $S_6 = 17.6$ , where the experimental solution

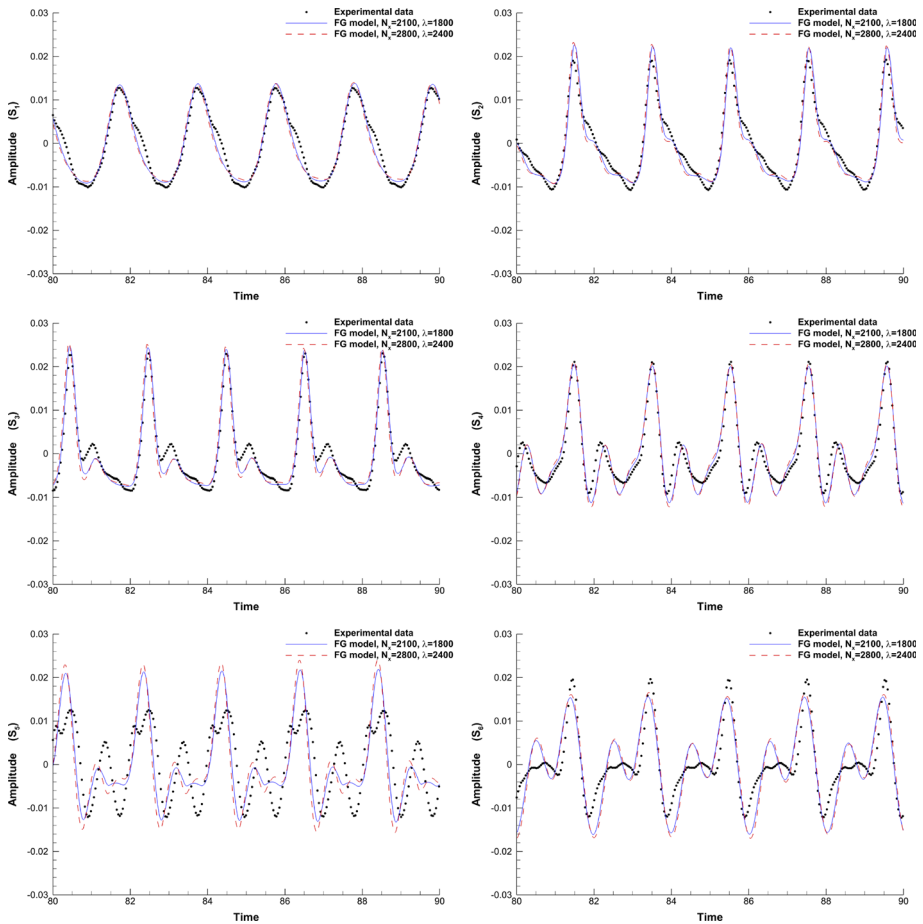


**Fig. 7** Time evolution of the wave amplitude  $A(t)$  for the low frequency periodic waves over a submerged bar test at wave gauges  $S_1 - S_6$ . Black dots correspond to experimental data [8], blue solid lines are the numerical results obtained for the model (1)–(5) using an ADER-DG scheme with  $N = 3$ , a mesh of 2100 elements and parameter  $\lambda = 1800$ ; the red dashed lines represent the solution for a mesh of 2800 elements and  $\lambda = 2400$  (Color figure online)

is available. The numerical results for the wave amplitude,  $A = h + b - \zeta_0$ , are reported in Fig. 7 for the low frequency case and in Fig. 8 for the high frequency test. For the low frequency case, two different mesh resolutions and two different values of  $\lambda$  have been used, in order to show that the obtained numerical results have already reached a good level of independence in terms of mesh spacing and  $\lambda$ . For the high frequency testcase, two different values of  $\lambda$  have been used in order to show that the chosen values of  $\lambda$  are large enough for practical simulations. The results are quite satisfactory and comparable with the ones obtained in [3]. The discrepancies, with respect to the experimental data, observed for  $S_5$  and  $S_6$  in LW may be due to the suboptimal linear dispersive properties of the model considered, see Sect. 2.1.2. To improve these results, models with better dispersion characteristics, like the Madsen & Sørensen model [77], may be employed in a future work.

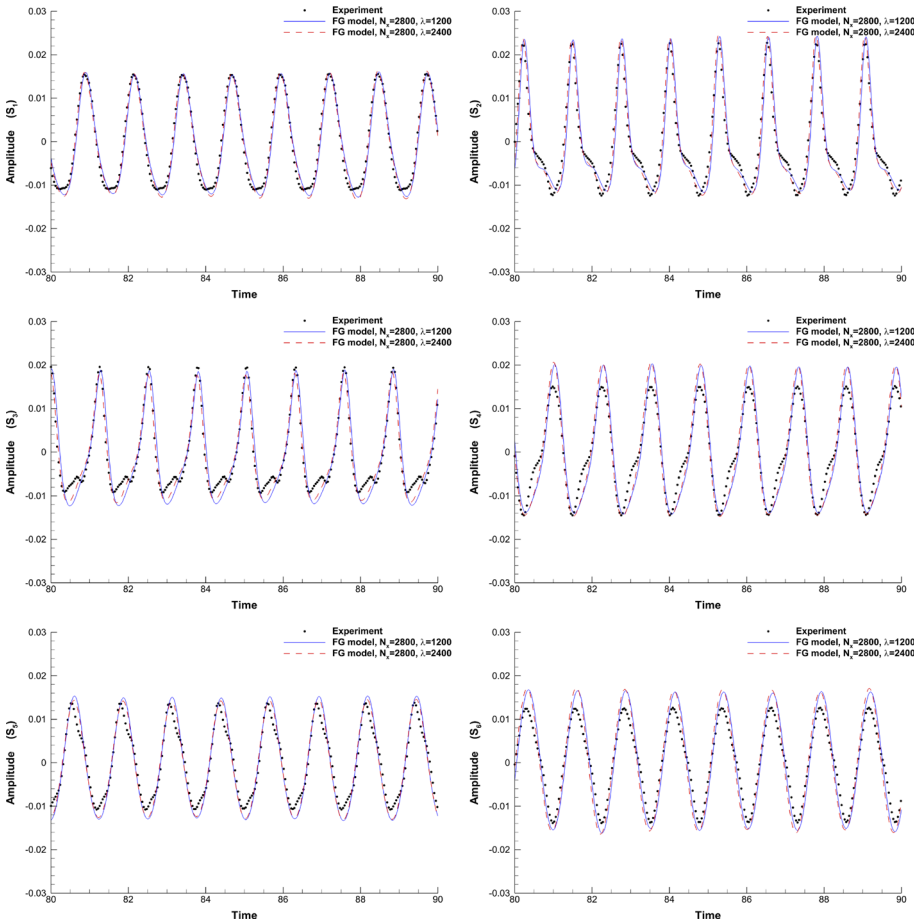


**Fig. 8** Time evolution of the wave amplitude  $A(t)$  for the high frequency periodic waves over a submerged bar test at wave gauges  $S_1 - S_6$ . Black dots correspond to experimental data [8], blue solid lines are the numerical results obtained for model [56] with variable bottom (1)–(5) using an ADER-DG scheme with  $N = 3$ , a mesh of 2800 elements and parameter  $\lambda = 1200$ ; red dashed lines are the solution for  $\lambda = 2400$  (Color figure online)

### 4.1.5 Favre Waves

In this section we consider the numerical simulation of so-called Favre waves, which are dispersive shock waves or undular bores developing when a fluid layer with a free surface hits against a wall, see [51,56] for numerical investigations and [102] for the corresponding experimental studies. The computational domain is  $\Omega = [-180, 0] \times [-1, +1]$  and it is covered by  $1200 \times 4$  ADER-DG elements of polynomial approximation degree  $N = 3$ . The initial condition for this test is

$$h = H, \quad \eta = H, \quad v_1 = \sqrt{gH} \left( F - \frac{1 + \sqrt{1 + 8F^2}}{4F} \right), \quad v_2 = w = b = 0 \quad (82)$$



where  $F$  is the relative Froude number of the impact velocity. As suggested in [56], instead of a wall at  $x = 0$  an alternative symmetric impact problem can also be considered. For the subsequent tests we choose the still water depth  $H = 1$  and the parameter  $\lambda$  is set to  $\lambda = 1200$ .

In order to capture the effect of *wave breaking*, only in this section the following simple wave breaking mechanism is employed, see [3,51]. For this purpose we modify the governing PDE for  $hw$  by adding a source term as follows:

$$\frac{\partial hw}{\partial t} + \frac{\partial}{\partial x_k} (hwv_k) = \lambda \left(1 - \frac{\eta}{h}\right) - 2\xi B hw, \tag{83}$$

with

$$B = \max \left(0, 1 - \frac{\partial_x(hv_1) + \partial_y(hv_2)}{U_1}\right) \left|\partial_x(hv_1) + \partial_y(hv_2)\right|, \tag{84}$$

$$U_1 = b_1\sqrt{gh}, \quad U_2 = b_2\sqrt{gh}, \tag{85}$$

and the switch function

$$\xi = \begin{cases} 0 & \text{if } \left|\partial_x(hv_1) + \partial_y(hv_2)\right| < U_2, \\ 1 & \text{if } \left|\partial_x(hv_1) + \partial_y(hv_2)\right| \geq U_2. \end{cases} \tag{86}$$

For our numerical tests we set  $b_1 = 0.5$  and  $b_2 = 0.25$ . In Fig. 9 we show the computational results obtained for Froude  $F = 1.15$  at a final time of  $t = 54$  using two different meshes, one with 1200 elements in  $x$  direction and a finer one with 2400 elements in  $x$  direction. We can note an excellent agreement of the two solutions with each other, showing that mesh convergence has been reached for this test. In Fig. 10 we compare our numerical results with the experimental data reported in [56,102]. The upper symbols refer to the amplitude of the first wave, while the lower symbols refer to the amplitude of the trough after the first wave. The agreement between numerical simulations and experimental data is very good up to  $F = 1.35$ , which is already in the range of Froude numbers where wave breaking occurs. This means that the simple wave breaking mechanism adopted here is valid at least for moderate Froude number flows with breaking waves.

### 4.1.6 Solitary Wave Run-Up onto a Plane Beach

Synolakis [95] carried out laboratory experiments for solitary incident waves to study propagation, breaking and run-up over a planar beach with a slope  $1 : 19.85$ . Since then, many researchers used his data to validate numerical models, as in [3,51–53,68,90,91], among others. Accordingly, this test case is here used to assess the capability of the proposed methodology to describe shoreline motions and wave breaking when it occurs. The bathymetry of the problem is described in Fig. 11. As initial condition we use the solitary wave solution of the genuinely SGN system given by (74)–(75) with

$$v_1 = 0, \quad w = -h\partial_x v_1, \quad \text{and } \eta = \frac{1}{2}h \left(1 + \sqrt{1 - \frac{12}{\lambda}p}\right) \tag{87}$$

where  $p$  is the non-hydrostatic pressure known for the SGN model. Note that for practical purposes, this analytical solution of the elliptic SGN model can be used as an approximate solution for the hyperbolised system.

The solitary wave of amplitude  $A = 0.3$  and  $H = 1$  is placed at the location  $x_{\text{sol}} = 25$ . The computational domain  $\Omega = [-10, +40] \times [-1, 1]$  is covered by  $200 \times 3$  ADER-DG

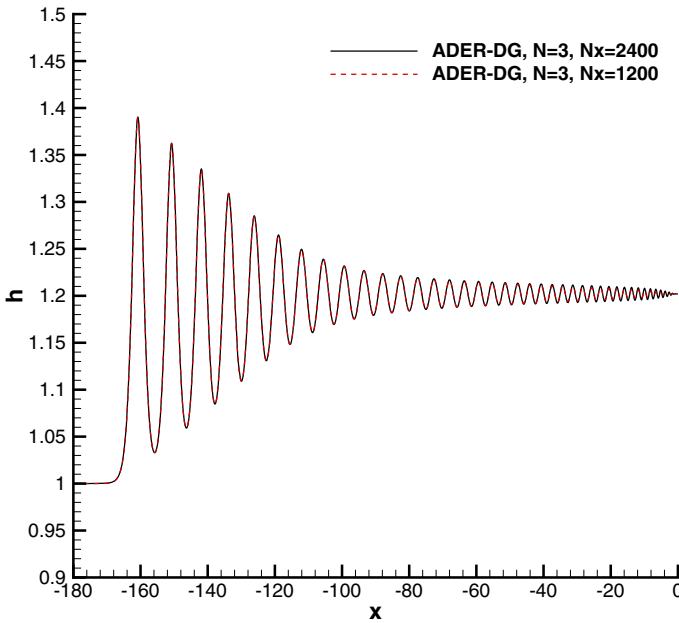


**Fig. 9** Favre waves at time  $t = 54$  for Froude number  $F = 1.15$ . Numerical results obtained for model (1)–(5) using an ADER-DG scheme with  $N = 3$  on a mesh composed of 1200 elements (dashed red line) and on a mesh composed of 2400 elements (solid black line) in  $x$  direction (Color figure online)

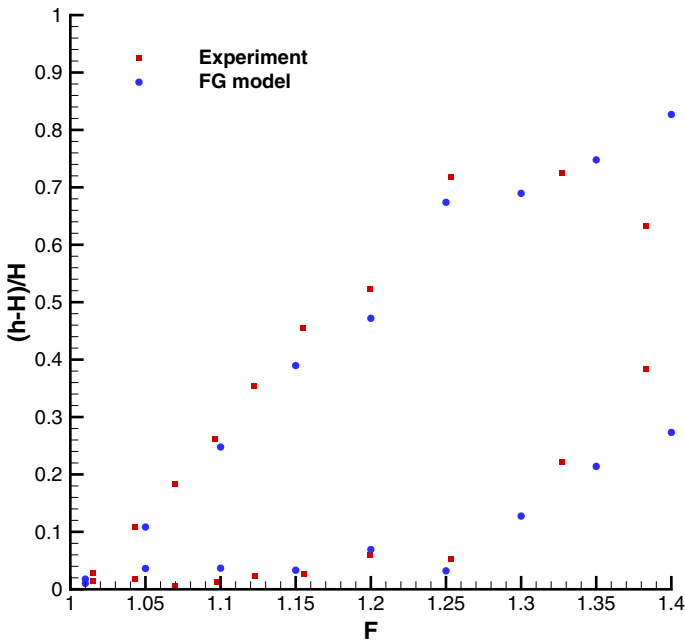


**Fig. 10** Favre waves. Comparison of the numerical results obtained with an ADER-DG scheme of polynomial approximation degree  $N = 3$  with the experimental data of [56,102]. For this test the simple wave breaking mechanism (83) has been employed

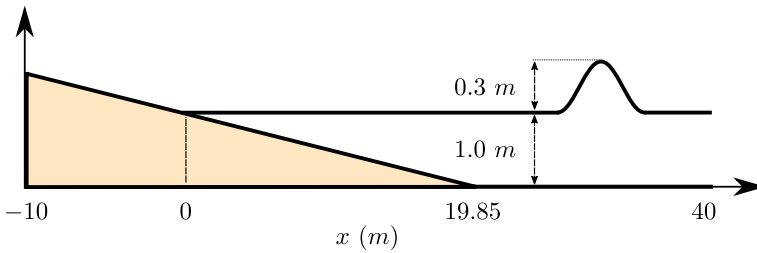


Fig. 11 Sketch of the bathymetry used for the solitary wave run-up onto a plane beach test

elements of polynomial approximation degree  $N = 3$ . For this test the simple wave breaking mechanism (83)–(85), with the same parameters  $b_1 = 0.5$ ,  $b_2 = 0.25$  has been employed. The relaxation speed  $\lambda$  is set to 1200. In order to take into account the glass surface roughness, the usual and simple bottom friction model used for the standard shallow-water equations is adopted via a usual Manning-type friction formula. For this purpose, we modify the governing equation for  $h v_i$  by adding a source term as follows:

$$\frac{\partial h v_i}{\partial t} + \frac{\partial}{\partial x} \left( h v_i v_k + \left( \frac{1}{2} g h^2 + h p \right) \delta_{ik} \right) + \left( g h + \frac{3 h}{2 \eta} p \right) \frac{\partial b}{\partial x_i} = -\tau_i,$$

with

$$\tau_i = n_m^2 g \frac{\sqrt{v_1^2 + v_2^2}}{h^{4/3}} v_i, \quad n_m = 4 \times 10^{-3}.$$

The *a posteriori* subcell finite volume limiter is activated in the presence of spurious oscillations as well as for small values of the total water depth  $h < 10^{-2}$ . Following [103], we employ a second-order scheme by using a TVD polynomial reconstruction procedure using the MUSCL slope limiter, which takes into account the positivity of the water height, [53], and the well-balancing for equilibrium. The time evolution stage to the half time level is then computed via a standard second-order TVD Runge-Kutta method, [61]. Finally, free-outflow boundary conditions are considered and the CFL number is set to 0.9.

Figure 12 depicts the snapshots at times  $t \in \{4.7, 6.3, 7.9, 9.5\}$ . Excellent results are obtained for the arrival time and the amplitude of the wave and for the maximum wave run-up, where the friction terms play an important role. This test shows that the proposed hyperbolic strategy, the chosen breaking mechanism, and the standard friction term from classical shallow water equations perform adequately for the proposed hyperbolic system.

#### 4.1.7 Solitary Wave Over a Gaussian Obstacle

This test run using the FG model is a solitary wave over a Gaussian obstacle in  $\Omega = [-5, +35] \times [-10, +10]$ . We consider the bathymetry given by

$$z_b(x, y) = A_g \exp \left( -\frac{x^2 + y^2}{2\sigma_g^2} \right), \tag{88}$$

where  $A_g = 0.1$  and  $\sigma_g = 1$ . The initial soliton is taken from Test 4.1.3,  $x_{sol} = -3$ ,  $A_i = 0.0365$ ,  $H = 0.2$ . We run a simulation on a mesh,  $M1$ , of  $200 \times 100$  elements with  $N = 3$ , final integration time  $t = 12$  and periodic boundary conditions everywhere. Since neither the exact solution nor experimental data is available, a mesh convergence study

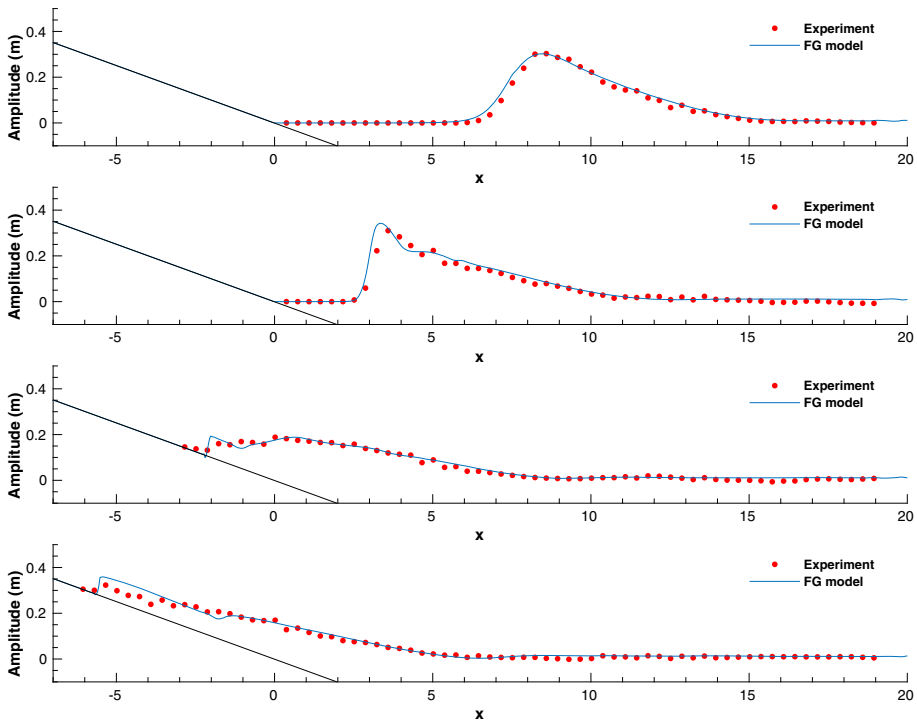


**Fig. 12** Comparison of the experimental data (dots) and the numerical results (solid blue line) obtained during the run-up at times  $t \in \{4.7, 6.3, 7.9, 9.5\}$  (from top to bottom) (Color figure online)

has been carried out by considering a refined mesh,  $M2$ , made of  $400 \times 200$  elements, using again  $N = 3$ . The 1D cut for the water depth at  $t = 12$  is reported in Fig. 13. The numerical solutions obtained on both meshes match perfectly, hence mesh convergence has been reached for this test. Figure 14 shows the snapshots of the free-surface  $A = h + b$  at different times,  $t \in \{0, 2, 5, 12\}$ . As expected, the soliton is propagated growing in amplitude in correspondence to the obstacle and generating a set of transmissive waves behind the main wave.

### 4.1.8 Solitary Wave Impinging on a Conical Island

A set of 2D experiments with solitary waves was carried out at the Coastal and Hydraulics Laboratory, Engineer Research and Development Center of the U.S. Army Corps of Engineers, [16]. The laboratory experiment consisted on an idealized representation of Babi Island in the Flores Sea, Indonesia. It should be mentioned that the waves generated in the laboratory are dispersive; hence, as many authors have already done, [51,74,105], it constitutes an almost ideal problem to test the accuracy of the model.

The computational domain  $\Omega = [-5, +25] \times [0, +30]$  is covered by  $150 \times 150$  ADER-DG elements of polynomial approximation degree  $N = 3$ . The still water depth is  $H = 0.32$  and a smoothed conical island centred at  $\mathbf{x}_{\text{obs}} = (12.96, 13.8)$  and base diameter  $d_{\text{obs}} = 7.2$

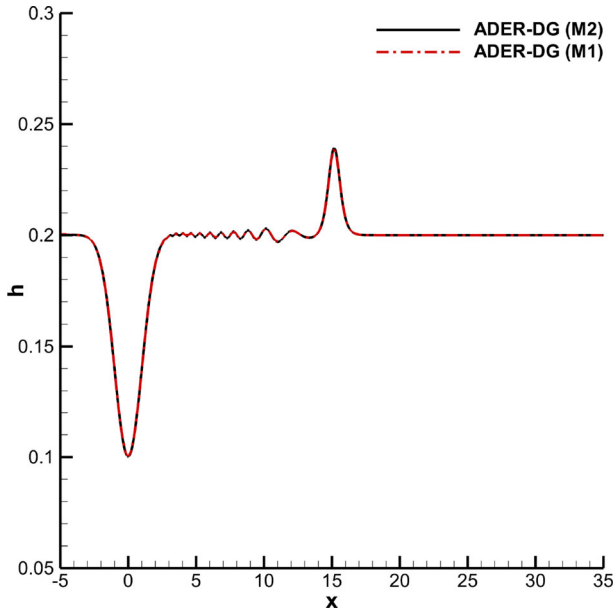


**Fig. 13** Solitary wave over a 2D Gaussian obstacle test. One-dimensional cut of the water depth,  $h$ , at  $t = 12$ . Mesh  $M1$ :  $\Delta x = \Delta y = 0.2$  (red dash-dotted line). Mesh  $M2$ :  $\Delta x = \Delta y = 0.1$  (black solid line) (Color figure online)

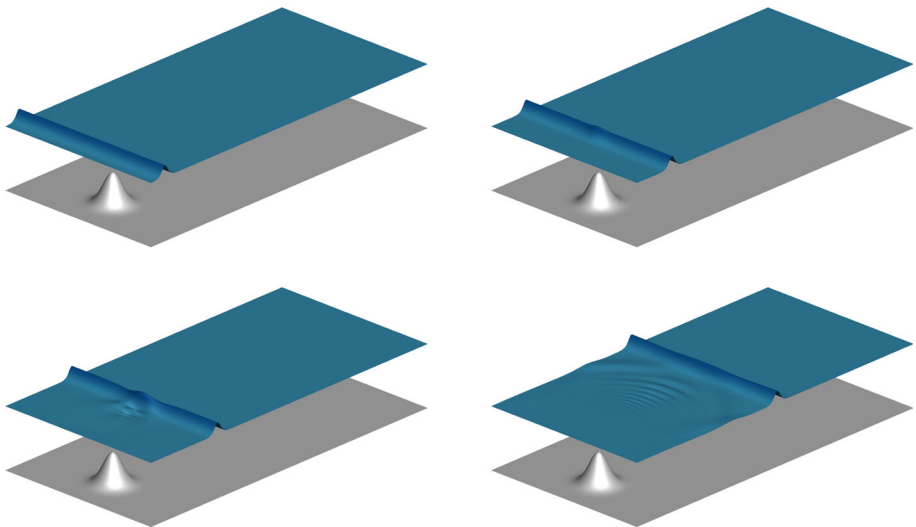


**Fig. 14** Snapshots of the free-surface  $A = h + b$  for the solitary wave over a 2D Gaussian obstacle test at times  $t \in \{0, 2, 5, 12\}$  with mesh  $M2$ . The bathymetry is represented in grey

given by

$$\begin{aligned} b(x, y) &= 0.33(1 + \tanh(d(x, y)/\zeta)) - H_0, \quad \zeta = 2.65, \quad H_0 = 0.32, \\ d(x, y) &= R_1 - \sqrt{3(x - x_0)^2 + 3(y - y_0)^2}, \quad R_1 = 3.6. \end{aligned} \quad (89)$$

Four wave gauges  $\mathbf{S}_1 = (9.36, 13.8)$ ,  $\mathbf{S}_2 = (10.36, 13.8)$ ,  $\mathbf{S}_3 = (12.96, 11.22)$ ,  $\mathbf{S}_4 = (15.56, 13.8)$ , are distributed around the island in order to measure the free surface elevation.

As done in Sect. 4.1.6, the initial condition for  $\rho$ ,  $v_i$ ,  $w$  and  $\eta$ , is a solitary wave of amplitude  $A = 0.06$ ,  $H = 0.32$  computed for the original SGN model and centred at  $x_{\text{sol}} = 0$ . The wave propagates until  $t = 15$  and the breaking mechanism is automatically activated with the same parameters than in all the previous numerical test,  $b_1 = 0.5$ ,  $b_2 = 0.25$ . The relaxation speed  $\lambda$  is set to 300. Since the model is constructed with smooth concrete, the friction with the topography is not considered here. Finally, free-outflow boundary conditions are considered and the CFL number is set to 0.9.

Similarly to the test in Sect. 4.1.6, the *a posteriori* subcell finite volume limiter is employed in the presence of spurious oscillations as well as for values of the total water depth smaller than  $10^{-1}$ . During the entire simulation, the subcell finite volume limiter was active for less than the 4 % of total elements of the computational domain. That ensures using a robust second-order scheme in a tiny part of the computational domain.

As expected, the approximated solution, Fig. 15, shows two wavefronts splitting in front of the island and colliding behind it. In Fig. 16, it can be found that, overall, the simulated water surface fluctuations agree well with the measured data for both the maximum amplitudes and the arrival time of the waves. Therefore, the proposed methodology seems to be able to reproduce measured wave propagation over an uneven 3D bottom accurately.

## 4.2 Hyperbolic Reformulation of the Nonlinear Schrödinger Equation

### 4.2.1 Numerical Convergence Study and Evolution of Curl Errors

In this section we use the stationary radial solution found in Sect. 2.2.2 in order to carry out a numerical convergence study of the high order ADER schemes proposed in this paper and in order to measure the errors in the involution constraint  $\nabla \times \mathbf{p}$  as a function of the GLM curl cleaning speed  $a_c$ .

The computational domain is given by  $\Omega = [-5, +5] \times [-5, +5]$  and is discretized with a uniform Cartesian mesh of  $N_x \times N_y$  DG elements of polynomial approximation degree  $N \in \{2, 3, 4, 5\}$ . All boundary conditions are periodic. The free parameters for the definition of the stationary vortex-type solution of Sect. 2.2.2 are defined as follows:  $\rho_0 = 2$ ,  $\hat{\rho} = 1$ ,  $L = 2$ ,  $p_0 = 0.1$ ,  $\sigma = 0.2$  and  $R = 1.5$ . The remaining parameters of the model are set to  $\beta = 1$ ,  $\lambda = 500$  and  $a_c = 20$ . Simulations are run until a final time of  $t = 0.25$  and the  $L^2$  errors of the numerical solution with respect to the exact one are reported in Table 4, together with the observed order of accuracy. From the obtained results we can conclude that, on sufficiently fine meshes, our high order ADER-DG schemes achieve a numerical convergence order of  $N$  to  $N + 1$  for all quantities.

We now run this test problem again for a longer time until  $t = 2$  using an ADER-DG scheme with  $N = 4$  on a uniform Cartesian mesh of  $N_x = N_y = 32$  elements and report the time series of the  $L^2$  error in the curl constraint  $\nabla \times \mathbf{p}$  for the original system (15)–(19) and of the augmented GLM system (35)–(40) as a function of the GLM cleaning speed  $a_c$ . From the results shown in Fig. 17 we can deduce that the curl errors decrease with increasing

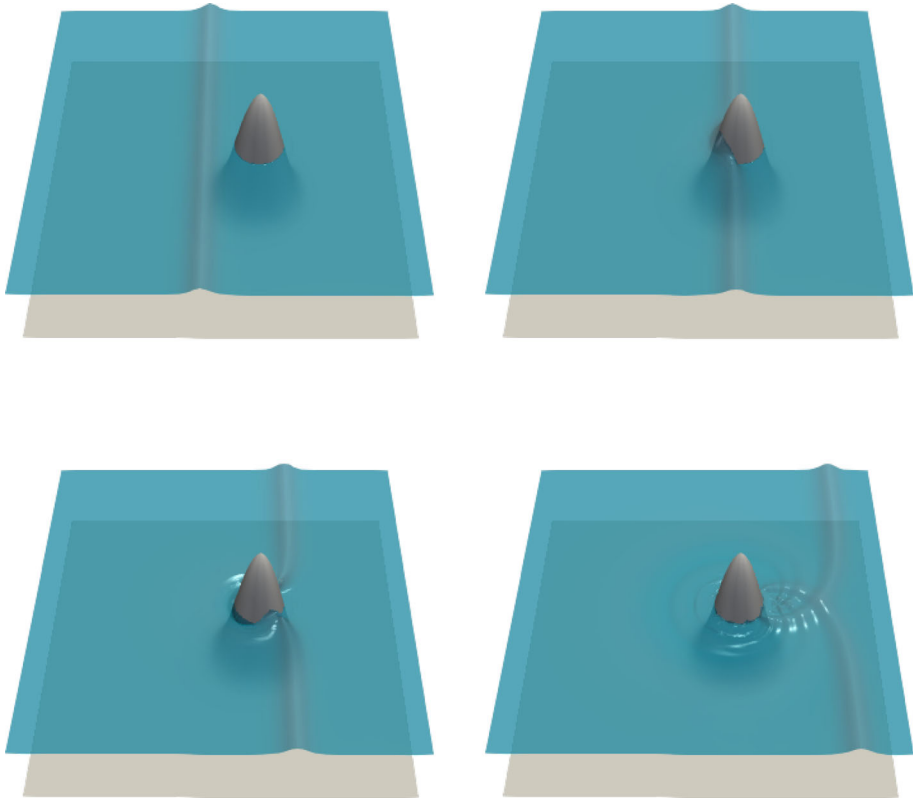


**Fig. 15** Snapshots of the free surface and bathymetry profile at times  $t \in \{4.5, 6.5, 8, 10\}$  (from top left to bottom right)

cleaning speed, as expected. A set of radial cuts through this stationary vortex-type problem is shown in Fig. 18, where the numerical solution obtained with the high order ADER-DG scheme is compared against the exact solution of the problem at time  $t = 2$ . We can note an excellent agreement between numerical and exact solution.

### 4.2.2 Gray Soliton

In this section we solve the gray soliton test problem, which was introduced and solved with second order TVD finite volume schemes in [38]. In this paper we employ very high order ADER-DG schemes instead. The initial condition is given by

$$\rho(x, 0) = b_1 - \frac{b_1 - b_3}{\cosh^2(\sqrt{b_1 - b_3}x)}, \quad v_1(x, 0) = U - \frac{b_1\sqrt{b_3}}{\rho(x, 0)}, \quad (90)$$

$$\eta(x, 0) = \rho(x, 0), \quad w(x, 0) = -\rho(x, 0)\partial_x v_1(x, 0), \quad p_1(x, 0) = \partial_x \rho(x, 0)$$

and  $v_2 = v_3 = p_2 = p_3 = 0$ . The computational domain is  $\Omega = [-20, +20] \times [0, +0.5]$  with periodic boundary conditions in all directions. The domain is discretized at the aid of  $1080 \times 10$  elements using an ADER-DG scheme of polynomial approximation degree  $N = 4$ .

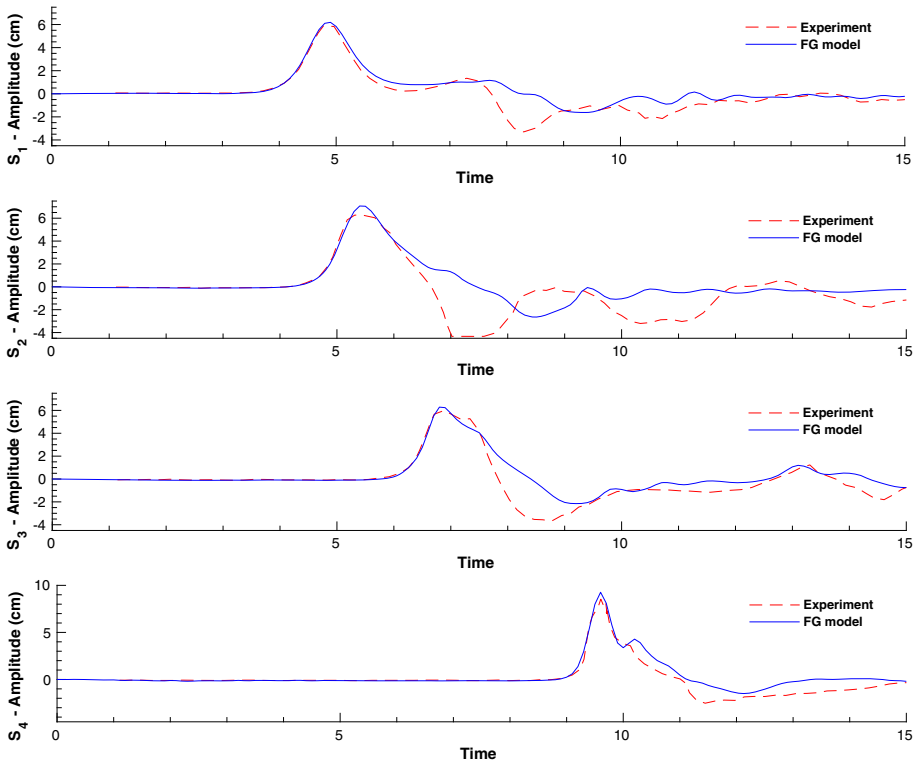


**Fig. 16** Comparison of the time evolution of the amplitude,  $A(t)$ , at wave gauges  $S_1 - S_4$  computed using the ADER-DG  $\mathbb{P}_3$  scheme (solid blue line) against the experimental data (dashed red line) for the solitary wave impinging on a conical island test (Color figure online)

According to [38] the parameters of the test problem are chosen as follows:  $b_1 = 1.5, b_3 = 1, U = 2$ , while the parameters of the hyperbolic model are set to  $\beta = 10^{-3}, \lambda = 2000$  and  $a_c = 0$ , since the test problem is one-dimensional. Simulations are run until a final time of  $t = 20$ , when the solitary wave has traveled one period through the domain and has returned to its initial location, so that the exact solution is given by the initial condition. A comparison of the high order ADER-DG solution and the exact solution is shown in Fig. 19. For all depicted variables, which are representative for the system, we can note an excellent agreement between the numerical solution and the exact one. Note that the nominally fifth order ADER-DG scheme with  $N = 4$  used in this paper needed only 5,400 degrees of freedom to resolve the solitary wave in  $x$  direction, while for the second order TVD scheme employed in [38] a very fine mesh composed of 200,000 elements in  $x$  direction was needed. The following  $L^2$  errors were measured at the final time  $t = 20$ : for the density,  $\rho$ , the error was  $6.0462 \cdot 10^{-3}$ , for the first velocity component,  $v_1$ , it was  $6.3848 \cdot 10^{-3}$ , for  $\eta$  it was  $6.0337 \cdot 10^{-3}$  and for  $p_1$  it was  $7.3374 \cdot 10^{-3}$ . These results clearly illustrate the benefit of very high order DG schemes for the numerical solution of hyperbolic reformulations of nonlinear dispersive systems over classical second order TVD finite volume schemes.



**Table 4** Numerical convergence results for high order ADER-DG schemes of polynomial approximation degree  $N \in \{2, 3, 4, 5\}$  for the hyperbolic reformulation of the Schrödinger equation (35)–(40) with a fixed cleaning speed of  $a_c = 20$  on a uniform Cartesian mesh composed of  $N_x = N_y$  elements. The  $L^2$  error norms and orders (in bold) refer to the variables  $\eta$ ,  $w$  and  $p_1$  at a final time of  $t = 0.25$

$N_x = N_y$	$L^2(\eta)$	$\mathcal{O}(\eta)$	$L^2(w)$	$\mathcal{O}(w)$	$L^2(p_1)$	$\mathcal{O}(p_1)$
<i>ADER-DG N = 2</i>						
16	7.5272E-02		2.7475E-01		1.2864E-01	
32	1.9211E-02	<b>2.0</b>	3.6952E-02	<b>2.9</b>	3.6686E-02	<b>1.8</b>
64	4.2150E-03	<b>2.2</b>	3.7878E-03	<b>3.3</b>	5.6467E-03	<b>2.7</b>
128	8.4925E-04	<b>2.3</b>	3.5474E-04	<b>3.4</b>	6.2646E-04	<b>3.2</b>
<i>ADER-DG N = 3</i>						
16	3.2089E-02		4.6461E-02		1.8055E-02	
32	2.9819E-03	<b>3.4</b>	2.3751E-03	<b>4.3</b>	3.6845E-03	<b>2.3</b>
64	1.1181E-04	<b>4.7</b>	7.7650E-05	<b>4.9</b>	2.0072E-04	<b>4.2</b>
128	4.5336E-06	<b>4.6</b>	2.0139E-06	<b>5.3</b>	4.6210E-06	<b>5.4</b>
<i>ADER-DG N = 4</i>						
16	4.0841E-03		6.1623E-03		5.7759E-03	
32	1.9832E-04	<b>4.4</b>	2.1044E-04	<b>4.9</b>	4.5919E-04	<b>3.7</b>
64	1.1167E-05	<b>4.2</b>	7.3094E-06	<b>4.8</b>	1.7988E-05	<b>4.7</b>
128	5.2303E-07	<b>4.4</b>	2.1548E-07	<b>5.1</b>	5.6020E-07	<b>5.0</b>
<i>ADER-DG N = 5</i>						
8	2.3465E-02		6.6136E-02		2.1526E-02	
16	1.1654E-03	<b>4.3</b>	1.5479E-03	<b>5.4</b>	2.1122E-03	<b>3.3</b>
32	4.5498E-05	<b>4.7</b>	3.0915E-05	<b>5.6</b>	4.7821E-05	<b>5.5</b>
64	4.3160E-07	<b>6.7</b>	3.3627E-07	<b>6.5</b>	7.2628E-07	<b>6.0</b>

### 4.2.3 Dispersive Shock in One Space Dimension

In order to verify our proposed numerical approach and its implementation also in the presence of dispersive shock waves, we first compare the numerical solution obtained with a fourth order ADER-DG scheme ( $N = 3$ ) in the domain  $\Omega = [-250, +250] \times [0, +25]$  on a uniform Cartesian mesh composed of  $10080 \times 4$  elements with the exact solution of the Whitham modulation equations that describe the temporal evolution of the envelope of the dispersive shock wave, see [38]. The parameters of the hyperbolic model are set to  $\beta = 2 \cdot 10^{-5}$ ,  $\lambda = 300$  and  $a_c = 0$ , since the test problem is one-dimensional. In Fig. 20 we show a comparison of numerical and exact solution for the fluid density  $\rho$  and for the velocity component  $v_1$  at a final time of  $t = 70$ . For both variables, an excellent agreement between the exact and the numerical solution can be observed for the envelope.

### 4.2.4 Dispersive Shock in Two Space Dimensions

Last but not least, we also carry out a qualitative comparison against experimental results in two dimensions. We start from a fluid initially at rest with  $\mathbf{v}_k = 0$ ,  $p_k = \partial_k \rho$ ,  $w = 0$  and

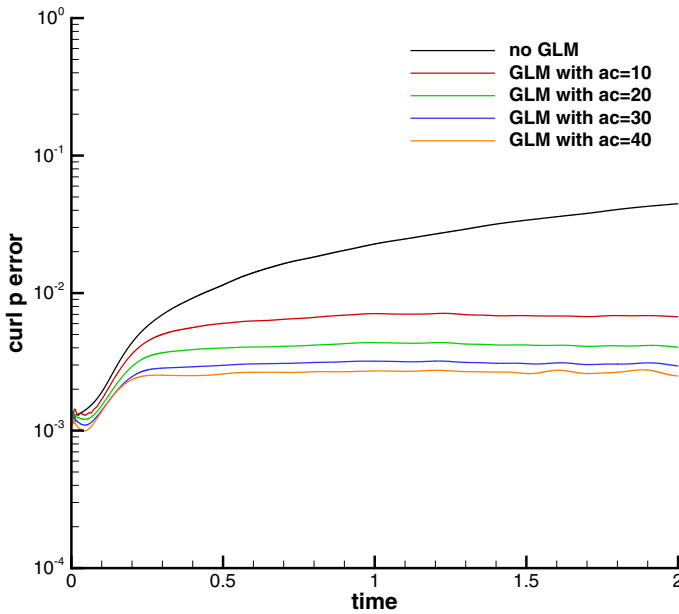


**Fig. 17** Time series of the  $L^2$  norm of the curl error in the vector field  $\mathbf{p}$  as a function of the GLM cleaning speed  $a_c$

$\eta = \rho$ . The initial density profile is given in terms of the radius  $r = \sqrt{x^2 + y^2}$  by

$$\rho(r, 0) = \frac{1}{2} (\rho_R + \rho_L) + \frac{1}{2} (\rho_R - \rho_L) \tanh\left(\frac{r - R}{\sigma}\right), \tag{91}$$

with  $\rho_L = 2$ ,  $\rho_R = 1$ ,  $R = 3$  and the smoothing parameter  $\sigma = 0.05$ . The computational domain  $\Omega = [-8, +8]^2$  is discretized with  $256 \times 256$  uniform Cartesian elements with polynomial approximation degree  $N = 3$  and simulations are run until a final time of  $t = 0.24$ . Also for this test case the parameters of the hyperbolic model with GLM curl cleaning are set to  $\beta = 2 \cdot 10^{-5}$ ,  $\lambda = 300$  and  $a_c = 20$ . In Fig. 21 we compare our numerical results against experimental observations published in [65] for a two-dimensional dispersive shock wave developing in a quantum fluid (Bose–Einstein Condensate—BEC). We can observe a good qualitative match between the two solutions.

### 5 Conclusion

In this paper we have focused on the solution of first order hyperbolic reformulations of nonlinear dispersive systems using a high order fully discrete one-step ADER discontinuous Galerkin methodology. Two different models derived from an extended Lagrangian variational principle have been considered. The hyperbolic reformulation of the Serre–Green–Naghdi model with flat bottom [56] has been extended to the 2D framework with variable bottom topography. The linear dispersion analysis reported in the present paper allows an easy comparison with other hyperbolic models of nonlinear dispersive water waves. As second system we have selected the defocusing nonlinear Schrödinger equation rewritten in the hyperbolic reformulation proposed in [38]. The extension of the original 1D model to the

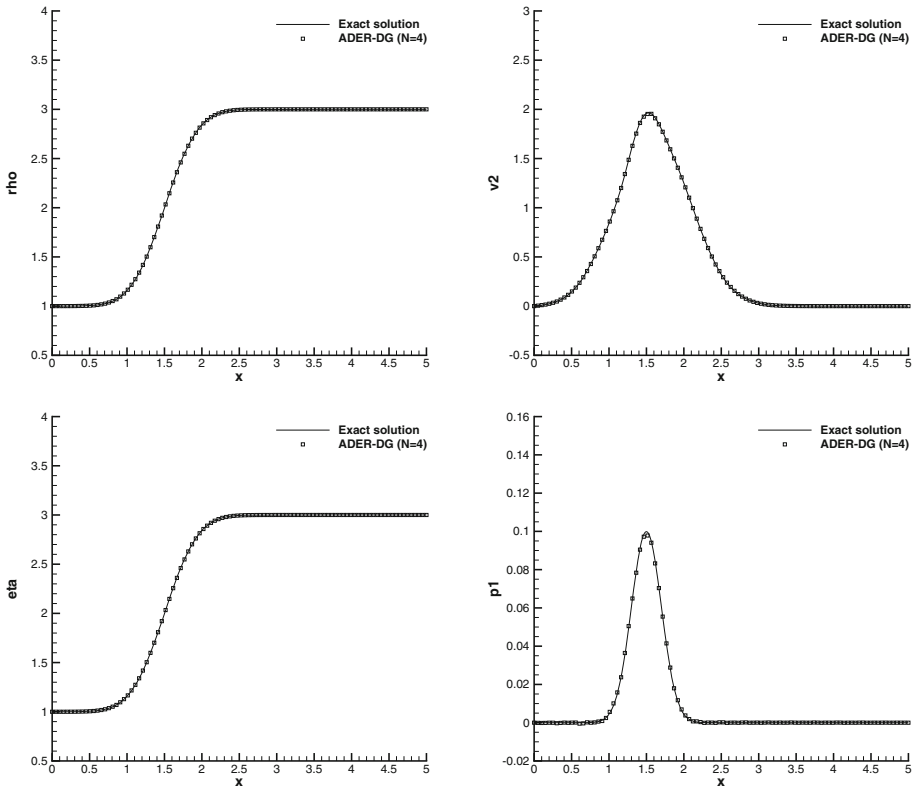


**Fig. 18** Radial cut through the numerical solution obtained with an ADER-DG scheme ( $N = 4$ ) on  $32 \times 32$  elements along the line  $y = 0$  and comparison with the exact solution at time  $t = 2$  for density  $\rho$  (top left), velocity component  $v_2$  (top right),  $\eta$  (bottom left) and  $p_1$  (bottom right)

multi-dimensional framework has shown the necessity of including a new term to restore the Galilean invariance of the system. Moreover, in this paper the model has also been augmented by a hyperbolic GLM curl cleaning approach so that we arrive at a structure preserving scheme that reduces the curl errors that are produced by the underlying numerical method. Let us note that, as an additional benefit of including the curl cleaning terms, the augmented system becomes strongly hyperbolic when the second and third components of the vector field  $\mathbf{p}$  are non zero, reverting to the eigenstructure of the original system in [38], which was only weakly hyperbolic in the multi-dimensional case in the absence of the GLM curl cleaning terms. The path-conservative ADER-DG methodology has been briefly recalled and combined with an *a posteriori* subcell finite volume limiter to avoid spurious oscillations in the numerical solution in the presence of discontinuities or strong gradients. For the hyperbolic model of nonlinear dispersive water waves (1)–(5) the well-balanced property of the employed path-conservative scheme has been rigorously proven for the case  $N = 0$  for arbitrary bottom topographies. A careful validation of the schemes has been carried out for both systems of equations showing numerical convergence tables of up to sixth order of accuracy. A set of numerical test has been run for each system including a comparison with exact and numerical reference solutions, as well as with available experimental data. The obtained results confirm the effectiveness of using very high order accurate numerical schemes against

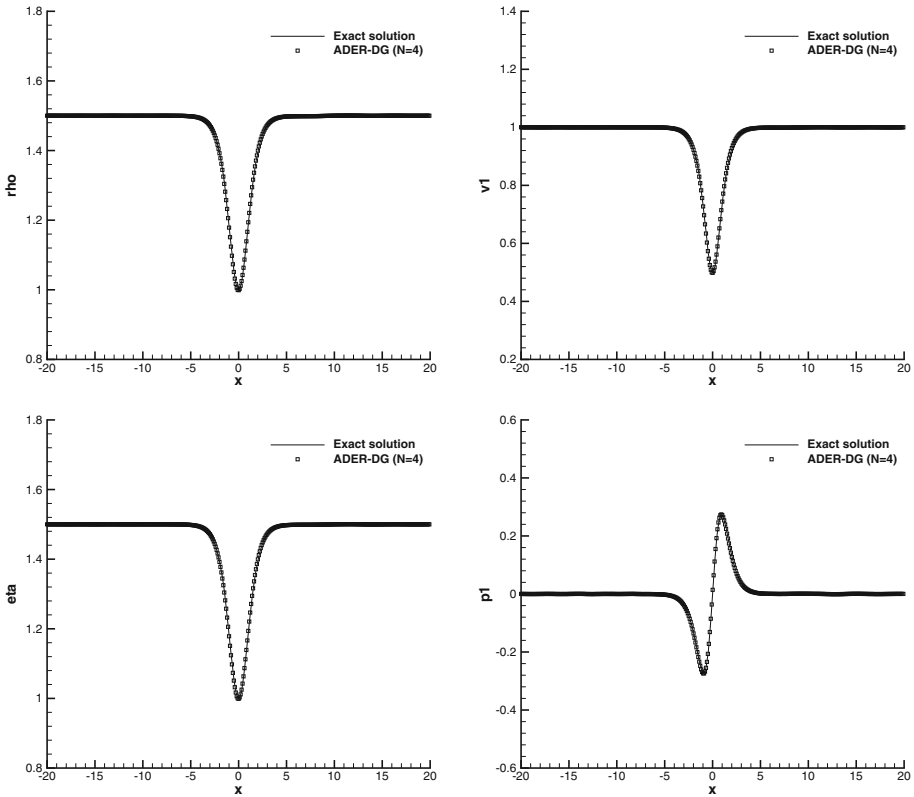


**Fig. 19** Exact and numerical solution for the gray soliton at time  $t = 20$ . Density  $\rho$  (top left), velocity component  $v_1$  (top right),  $\eta$  (bottom left) and  $p_1$  (bottom right)

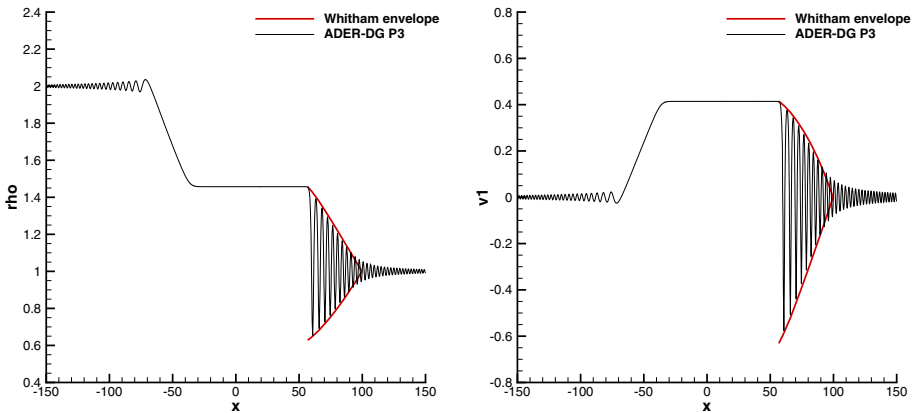


**Fig. 20** Solution of a dispersive Riemann problem of the hyperbolic reformulation of the Schrödinger equation [38] and comparison with the exact solution of the Whitham modulation equations for the envelope of the curve at time  $t = 70$ . Fluid density (left) and velocity component  $v_1$  (right)

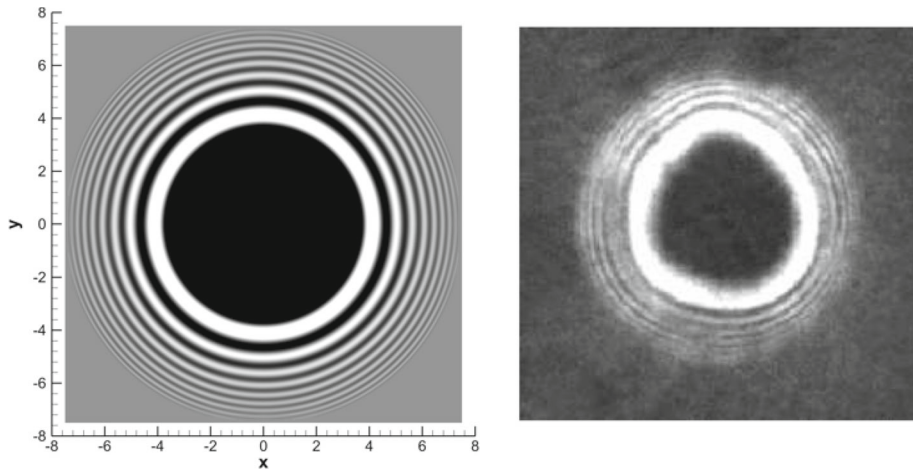


**Fig. 21** Density contours at  $t = 0.24$  for a *dispersive shock wave* in 2D. Simulation of the hyperbolic reformulation of the Schrödinger equation with a fourth order ADER-DG scheme (left) and experimental results of [65] obtained for a dispersive shock wave in a Bose–Einstein condensate (right)

classical low order finite volume methods which, even in the one-dimensional case, require a very fine grid leading to a prohibitive computational cost in higher space dimensions.

In the future, we plan to apply the numerical method developed in this paper also to other nonlinear dispersive systems, such as the Navier-Stokes-Korteweg system, for which a hyperbolic reformulation is possible by combining the GPR model of continuum mechanics [17,47,88] with the hyperbolic reformulation of the nonlinear Schrödinger equation introduced in [38] and studied in the present paper. As further research, we also plan to develop novel *structure-preserving* semi-implicit schemes on staggered meshes to solve the systems under investigation in this paper, following the ideas outlined in [9,11,18,19], with the aim to preserve the curl constraint *exactly* at the discrete level.

**Acknowledgements** The research presented in this paper has been financed by the European Union’s Horizon 2020 Research and Innovation Programme under the Project *ExaHyPE*, Grant no. 671698 (call FETHPC-1-2014). S.B. and M.D. are both members of the INdAM GNCS group and acknowledge the financial support received from the Italian Ministry of Education, University and Research (MIUR) in the frame of the Departments of Excellence Initiative 2018–2022 attributed to DICAM of the University of Trento (Grant L. 232/2016) and in the frame of the PRIN 2017 Project *Innovative numerical methods for evolutionary partial differential equations and applications*. S.B. was also funded by INdAM via a GNCS Grant for young researchers. N.F. and S.G. were partially funded by the Excellence Initiative of Aix-Marseille University—A\*Midex, a French “Investissements d’Avenir programme” AMX-19-IET-010, and the Russian Science Foundation (Project 20-11-20189).

**Funding** Open access funding provided by Università degli Studi di Trento within the CRUI-CARE Agreement.

**Open Access** This article is licensed under a Creative Commons Attribution 4.0 International License, which permits use, sharing, adaptation, distribution and reproduction in any medium or format, as long as you give appropriate credit to the original author(s) and the source, provide a link to the Creative Commons licence, and indicate if changes were made. The images or other third party material in this article are included in the article’s Creative Commons licence, unless indicated otherwise in a credit line to the material. If material is not included in the article’s Creative Commons licence and your intended use is not permitted by statutory regulation or exceeds the permitted use, you will need to obtain permission directly from the copyright holder. To view a copy of this licence, visit <http://creativecommons.org/licenses/by/4.0/>.

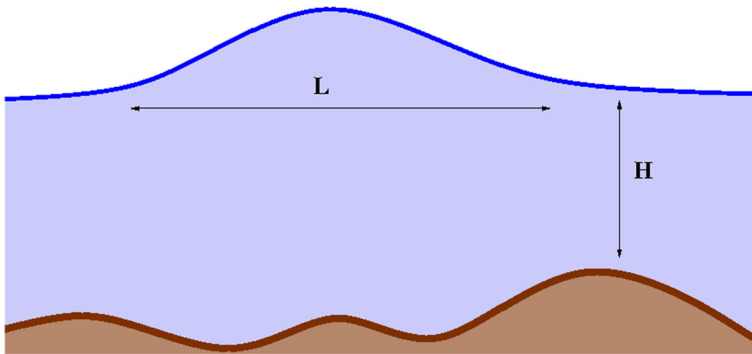


Fig. 22 A sketch of the flow over topography

### A Appendix

The hyperbolic version of the Serre–Green–Naghdi equations was derived in [56] only in the case of a flat bottom. Here we present the model derivation for the flows over topography. Consider the Euler equations of incompressible fluids between the rigid bottom described by  $z = b(t, x_1, x_2)$  and the free surface  $z = h(t, x_1, x_2) + b(t, x_1, x_2)$  :

$$\operatorname{div}_2 \mathbf{v} + \frac{\partial v_3}{\partial z} = 0, \quad \rho \frac{D\mathbf{v}}{Dt} + \nabla_2 p = 0, \quad \rho \frac{Dv_3}{Dt} + \frac{\partial p}{\partial z} = -\rho g \tag{92}$$

where  $(\mathbf{v}, v_3)^T$  is the velocity field,  $\mathbf{v} = (v_1, v_2)^T$  is the horizontal velocity,  $v_3$  is the vertical component of the velocity,  $g$  is the gravity acceleration, the divergence and the gradient are taken with respect to  $x_1, x_2$  (this is denoted with index 2);  $\rho$  is the fluid density,  $p$  is the pressure,  $\frac{D}{Dt} = \frac{\partial}{\partial t} + \mathbf{v} \cdot \nabla_2 + v_3 \frac{\partial}{\partial z}$  is the material derivative. The standard boundary conditions are fulfilled at the free surface:

$$(h + b)_t + \mathbf{v} \cdot \nabla_2 (h + b) = v_3, \quad p = 0, \tag{93}$$

and at the bottom

$$b_t + \mathbf{v} \cdot \nabla_2 b = v_3. \tag{94}$$

In the shallow water approximation the dimensionless equations become (we will use the same notations for dimensionless variables):

$$\operatorname{div}_2 \mathbf{v} + \frac{\partial v_3}{\partial z} = 0, \quad \frac{D\mathbf{v}}{Dt} + \nabla_2 p = 0, \quad \varepsilon^2 \frac{Dv_3}{Dt} + \frac{\partial p}{\partial z} = -1. \tag{95}$$

Here the small parameter  $\varepsilon = H/L$  represents the ratio of the vertical and horizontal scales (see Fig. 22).

The corresponding total energy of the flow can be written as

$$\mathcal{E} = \int_{-\infty}^{+\infty} \int_{-\infty}^{+\infty} \int_b^{b+h} \left( \frac{|\mathbf{v}|^2 + \varepsilon^2 v_3^2}{2} + z + C \right) dz dx_1 dx_2 \tag{96}$$

where the constant  $C$  is added to have a finite total energy in the class of solutions having the same constant values at infinity ( $\mathbf{v} \rightarrow \mathbf{0}, h \rightarrow h_\infty, b \rightarrow 0$ ). Obviously, this constant  $C$  does

not influence the corresponding Euler-Lagrange equations. The incompressibility equation and kinematic boundary conditions imply the mass conservation law in the form

$$h_t + \operatorname{div}(h\bar{\mathbf{v}}) = 0, \quad h\bar{\mathbf{v}} = \int_b^{b+h} \mathbf{v} dz. \tag{97}$$

In the following, ‘dot’ means the material derivative along the average velocity. For example,

$$\dot{h} = \frac{\partial h}{\partial t} + \bar{\mathbf{v}} \cdot \nabla_2 h. \tag{98}$$

Under additional assumption –the vorticity is of order  $\varepsilon^\beta$ , with  $\beta > 1$ – one can easily obtain (see [2] for details)

$$v_3 \approx \dot{b} - (z - b)\operatorname{div}\bar{\mathbf{v}} = \dot{b} + \frac{z - b}{h}\dot{h}. \tag{99}$$

Then, up to  $\varepsilon^2$  order terms one has [2]:

$$\int_b^{b+h} \left( \frac{|\mathbf{v}|^2 + \varepsilon^2 v_3^2}{2} + z \right) dz \approx h \left( \frac{|\bar{\mathbf{v}}|^2}{2} + \frac{\varepsilon^2}{6} \left( \dot{h} + \frac{3}{2}\dot{b} \right)^2 + \frac{\varepsilon^2}{8}\dot{b}^2 \right) + \frac{h}{2}(2b + h). \tag{100}$$

It allows us to write the Lagrangian in the form (we return back to the dimension variables):

$$\mathcal{L} = \int_{-\infty}^{+\infty} \int_{-\infty}^{+\infty} L dx_1 dx_2,$$

with

$$L(\bar{\mathbf{v}}, h, \dot{h}, b, \dot{b}) = \left( h \left( \frac{|\bar{\mathbf{v}}|^2}{2} + \frac{1}{6} \left( \dot{h} + \frac{3}{2}\dot{b} \right)^2 + \frac{1}{8}\dot{b}^2 \right) - \frac{gh}{2}(h + 2b) - Ch \right).$$

The corresponding Hamilton’s action between the time instant  $t_0$  and  $t_1$  is then

$$a = \int_{t_0}^{t_1} \mathcal{L} dt. \tag{101}$$

The Euler-Lagrange equations for (101) are obtained under the mass conservation constraint (97). Following [56], the extended Lagrangian is defined as

$$\hat{\mathcal{L}} = \int_{-\infty}^{+\infty} \int_{-\infty}^{+\infty} \hat{L} dx_1 dx_2,$$

with

$$\hat{L}(\bar{\mathbf{v}}, h, \eta, \dot{\eta}, b, \dot{b}) = \left( h \left( \frac{|\bar{\mathbf{v}}|^2}{2} + \frac{1}{6} \left( \dot{\eta} + \frac{3}{2}\dot{b} \right)^2 + \frac{1}{8}\dot{b}^2 \right) - \frac{gh}{2}(h + 2b) - \frac{\lambda h}{6} \left( \frac{\eta}{h} - 1 \right)^2 - Ch \right). \tag{102}$$

Here  $\lambda$  is a large constant having the dimension of squared velocity. The corresponding variational technique to find the Euler–Lagrange equations can be found in [36], [38]. The obtained governing equations are yet quite complicated for the numerical study and contain non-conservative products. We simplify now the Lagrangian (102) under the hypothesis that

the bottom is immobile,  $b = b(x_1, x_2)$ , hence  $\dot{b} = \bar{\mathbf{v}} \cdot \nabla_2 b$ , and the gradients of  $b$  are small ('mild' bottom approximation). So, a family of equivalent Lagrangians, defined up to  $\dot{b}^2$  terms, can be considered. We take the Lagrangian in the form

$$\hat{L} \approx \hat{L}_m = h \left( \frac{|\bar{\mathbf{v}}|^2}{2} + \frac{1}{6} \left( \dot{\eta} + \frac{3}{2} \dot{b} \right)^2 - \frac{g}{2} (h + 2b) - \frac{\lambda}{6} \left( \frac{\eta}{h} - 1 \right)^2 - C \right). \tag{103}$$

The variation of  $\hat{L}_m$  with respect to  $\eta$  gives us a second order equation which can be re-written as a system of two first order equations

$$\dot{\eta} = w - \frac{3}{2} \dot{b}, \quad \dot{w} = \frac{\lambda}{h} \left( 1 - \frac{\eta}{h} \right). \tag{104}$$

The momentum equation requires a little bit longer but straightforward calculations, [36], [38]:

$$\frac{\partial (h\bar{\mathbf{v}})}{\partial t} + \text{div}_2 (h\bar{\mathbf{v}} \otimes \bar{\mathbf{v}}) + \nabla P + \left( gh + \frac{\lambda}{2} \left( 1 - \frac{\eta}{h} \right) \right) \nabla b = 0, \tag{105}$$

with

$$P = \frac{gh^2}{2} + \frac{\lambda}{3} \eta \left( 1 - \frac{\eta}{h} \right).$$

The system (104), (105) complemented by the mass equation (97) obviously admits the energy conservation law (Noether theorem):

$$\frac{\partial}{\partial t} \left( h \left( \frac{|\bar{\mathbf{v}}|^2}{2} + e \right) \right) + \text{div}_2 \left( h\bar{\mathbf{v}} \left( \frac{|\bar{\mathbf{v}}|^2}{2} + e \right) + P\bar{\mathbf{v}} \right) = 0, \tag{106}$$

with

$$e = \frac{1}{6} \left( \dot{\eta} + \frac{3}{2} \dot{b} \right)^2 + \frac{g}{2} (h + 2b) + \frac{\lambda}{6} \left( \frac{\eta}{h} - 1 \right)^2. \tag{107}$$

Indeed, (106)–(107) imply

$$\begin{aligned} & h(\bar{\mathbf{v}} \cdot \dot{\bar{\mathbf{v}}} + \dot{e}) + \nabla P \cdot \bar{\mathbf{v}} - P \frac{\dot{h}}{h} \\ &= - \left( gh + \frac{\lambda}{2} \left( 1 - \frac{\eta}{h} \right) \right) \dot{b} + h\dot{e} - P \frac{\dot{h}}{h} \\ &= - \left( gh + \frac{\lambda}{2} \left( 1 - \frac{\eta}{h} \right) \right) \dot{b} \\ &\quad + h \left( \frac{1}{3} \left( \dot{\eta} + \frac{3}{2} \dot{b} \right) \left( \dot{\eta} + \frac{3}{2} \dot{b} \right) + \frac{g}{2} (\dot{h} + 2\dot{b}) + \frac{\lambda}{3} \left( \frac{\eta}{h} - 1 \right) \left( \frac{\dot{\eta}}{h} - \frac{\eta\dot{h}}{h^2} \right) \right) - P \frac{\dot{h}}{h} \\ &= - \left( gh + \frac{\lambda}{2} \left( 1 - \frac{\eta}{h} \right) \right) \dot{b} \\ &\quad + h \left( \frac{\lambda}{3h} \left( \dot{\eta} + \frac{3}{2} \dot{b} \right) \left( 1 - \frac{\eta}{h} \right) + \frac{g}{2} (\dot{h} + 2\dot{b}) + \frac{\lambda}{3} \left( \frac{\eta}{h} - 1 \right) \left( \frac{\dot{\eta}}{h} - \frac{\eta\dot{h}}{h^2} \right) \right) - P \frac{\dot{h}}{h} \\ &= h \left( \frac{\lambda}{3h} \dot{\eta} \left( 1 - \frac{\eta}{h} \right) + \frac{g}{2} \dot{h} + \frac{\lambda}{3} \left( \frac{\eta}{h} - 1 \right) \left( \frac{\dot{\eta}}{h} - \frac{\eta\dot{h}}{h^2} \right) \right) - P \frac{\dot{h}}{h} \\ &= \frac{gh}{2} \dot{h} - \frac{\lambda}{3} \left( \frac{\eta}{h} - 1 \right) \frac{\eta\dot{h}}{h} - \left( \frac{gh^2}{2} + \frac{\lambda}{3} \eta \left( 1 - \frac{\eta}{h} \right) \right) \frac{\dot{h}}{h} = 0. \end{aligned}$$



To simplify notations, we will further suppress ‘bar’ in the definition of the average velocity. For convenience, the total ‘pressure’  $P$  will be presented as the sum of the hydrostatic and non-hydrostatic part:

$$P = \frac{gh^2}{2} + hp(h, \eta), \quad p(h, \eta) = \frac{\lambda}{3} \frac{\eta}{h} \left(1 - \frac{\eta}{h}\right).$$

## B Appendix

The hyperbolic reformulation of the nonlinear Schrödinger equation obtained by the extended Lagrangian method, [38], reads

$$\frac{\partial \rho}{\partial t} + \operatorname{div}(\rho \mathbf{v}) = 0, \tag{108}$$

$$\frac{\partial \rho \mathbf{v}}{\partial t} + \operatorname{div} \left( \rho \mathbf{v} \otimes \mathbf{v} + P \mathbf{I} + \frac{1}{4\rho} \mathbf{p} \otimes \mathbf{p} \right) = 0, \tag{109}$$

$$\frac{\partial \rho \eta}{\partial t} + \operatorname{div}(\rho \eta \mathbf{v}) = \rho w, \tag{110}$$

$$\frac{\partial \rho w}{\partial t} + \operatorname{div} \left( \rho w \mathbf{v} - \frac{1}{4\rho\beta} \mathbf{p} \right) = \frac{\lambda}{\beta} \left(1 - \frac{\eta}{\rho}\right), \tag{111}$$

$$\frac{\partial \mathbf{p}}{\partial t} + \nabla \cdot (\mathbf{p} \cdot \mathbf{v} - w) + \left( \frac{\partial \mathbf{p}}{\partial \mathbf{x}} - \left( \frac{\partial \mathbf{p}}{\partial \mathbf{x}} \right)^T \right) \mathbf{v} = 0, \tag{112}$$

$$\nabla \times \mathbf{p} = 0, \tag{113}$$

with the pressure

$$P = \frac{1}{2} \rho^2 - \frac{1}{4\rho} |\mathbf{p}|^2 + \lambda \eta \left(1 - \frac{\eta}{\rho}\right).$$

Here  $\lambda \gg 1$  and  $\beta \ll 1$  are two free parameters which make the system (108)–(113) tend to the original hydrodynamic model of the Schrödinger equation in the limit  $\lambda \rightarrow \infty$  and  $\beta \rightarrow 0$ . Compared to [38] the governing equation for  $\mathbf{p}$  is *different* in this paper, in order to restore the *Galilean invariance* of the system, see [27,47,60,92]. Obviously, if initially  $\nabla \times \mathbf{p} = 0$ , it will be zero for any time. The equations for  $w, \eta$  and  $\mathbf{p}$  can also be written in non-conservative form:

$$\dot{\eta} = w, \quad \rho\beta\dot{w} = \operatorname{div} \left( \frac{\mathbf{p}}{4\rho} \right) + \lambda \left(1 - \frac{\eta}{\rho}\right), \quad \dot{\mathbf{p}} + \left( \frac{\partial \mathbf{v}}{\partial \mathbf{x}} \right)^T \mathbf{p} - \nabla w = 0, \tag{114}$$

where the ‘dot’ denotes the material time derivative. Equations (108)–(113) admit the energy conservation law:

$$E = \frac{\partial}{\partial t} \left( \rho \left( e + \frac{|\mathbf{v}|^2}{2} \right) \right) + \operatorname{div} \left( \rho \mathbf{v} \left( e + \frac{|\mathbf{v}|^2}{2} \right) + \Pi \mathbf{v} - \frac{1}{4\rho} w \mathbf{p} \right) = 0,$$

with  $\Pi = P \mathbf{I} + \frac{1}{4\rho} \mathbf{p} \otimes \mathbf{p}$  and  $e = \frac{\beta}{2} \dot{\eta}^2 + \frac{\rho}{2} + \frac{1}{4\rho^2} \frac{|\mathbf{p}|^2}{2} + \frac{\lambda}{2} \left( \frac{\eta}{\rho} - 1 \right)^2$ .

Indeed,

$$E = \rho (\dot{e} + \mathbf{v} \cdot \dot{\mathbf{v}}) + \operatorname{div} \Pi \mathbf{v} + \operatorname{tr} \left( \Pi \frac{\partial \mathbf{v}}{\partial \mathbf{x}} \right) - \frac{\mathbf{p}}{4\rho} \cdot \nabla w - \operatorname{div} \left( \frac{\mathbf{p}}{4\rho} \right) w$$

$$\begin{aligned}
 &= \rho \dot{e} + \text{tr} \left( \Pi \frac{\partial \mathbf{v}}{\partial \mathbf{x}} \right) - \frac{\mathbf{p}}{4\rho} \cdot \nabla w - \text{div} \left( \frac{\mathbf{p}}{4\rho} \right) w \\
 &= \rho \dot{e} + P \text{div} \mathbf{v} + \frac{1}{4\rho} \mathbf{p}^T \frac{\partial \mathbf{v}}{\partial \mathbf{x}} \mathbf{p} - \frac{\mathbf{p}}{4\rho} \cdot \nabla w - \text{div} \left( \frac{\mathbf{p}}{4\rho} \right) w \\
 &= \rho \left( \beta \dot{\eta} \ddot{\eta} + \frac{\dot{\rho}}{2} + \frac{1}{4} \frac{\mathbf{p}}{\rho} \cdot \left( \frac{\dot{\mathbf{p}}}{\rho} - \frac{\mathbf{p}}{\rho^2} \dot{\rho} \right) + \lambda \left( \frac{\eta}{\rho} - 1 \right) \left( \frac{\dot{\eta}}{\rho} - \frac{\eta}{\rho^2} \dot{\rho} \right) \right) \\
 &\quad - \left( \frac{1}{2} \rho^2 - \frac{1}{4\rho} |\mathbf{p}|^2 + \lambda \eta \left( 1 - \frac{\eta}{\rho} \right) \right) \frac{\dot{\rho}}{\rho} + \frac{1}{4\rho} \mathbf{p}^T \frac{\partial \mathbf{v}}{\partial \mathbf{x}} \mathbf{p} - \frac{\mathbf{p}}{4\rho} \cdot \nabla w - \text{div} \left( \frac{\mathbf{p}}{4\rho} \right) w.
 \end{aligned}$$

Using (114), one can see that  $E$  identically vanishes.

Now, let us add additional ‘blue terms’ into our system for the curl-cleaning:

$$\frac{\partial \rho}{\partial t} + \text{div} (\rho \mathbf{v}) = 0, \tag{115}$$

$$\frac{\partial \rho \mathbf{v}}{\partial t} + \text{div} \left( \rho \mathbf{v} \otimes \mathbf{v} + P \mathbf{I} + \frac{1}{4\rho} \mathbf{p} \otimes \mathbf{p} \right) = 0, \tag{116}$$

$$\frac{\partial \rho \eta}{\partial t} + \text{div} (\rho \eta \mathbf{v}) = \rho w, \tag{117}$$

$$\frac{\partial \rho w}{\partial t} + \text{div} \left( \rho w \mathbf{v} - \frac{1}{4\rho \beta} \mathbf{p} \right) = \frac{\lambda}{\beta} \left( 1 - \frac{\eta}{\rho} \right), \tag{118}$$

$$\frac{\partial \mathbf{p}}{\partial t} + \nabla (\mathbf{p} \cdot \mathbf{v} - w) + \left( \frac{\partial \mathbf{p}}{\partial \mathbf{x}} - \left( \frac{\partial \mathbf{p}}{\partial \mathbf{x}} \right)^T \right) \mathbf{v} + A_p \nabla \times \boldsymbol{\psi} = 0, \tag{119}$$

$$\dot{\boldsymbol{\psi}} - A_\psi \nabla \times \mathbf{p} = 0 \tag{120}$$

where the coefficients  $A_p$  and  $A_\psi$  should be chosen in such a way that the energy equation is satisfied. The equations for  $w$ ,  $\eta$  and  $\mathbf{p}$  can be rewritten again in non-conservative form:

$$\begin{aligned}
 \dot{\eta} &= w, \quad \rho \beta \dot{w} = \text{div} \left( \frac{\mathbf{p}}{4\rho} \right) + \lambda \left( 1 - \frac{\eta}{\rho} \right), \\
 \dot{\mathbf{p}} + \left( \frac{\partial \mathbf{v}}{\partial \mathbf{x}} \right)^T \mathbf{p} - \nabla w + A_p \nabla \times \boldsymbol{\psi} &= 0.
 \end{aligned} \tag{121}$$

Equations (115)–(120) admit the energy conservation law in the form:

$$\begin{aligned}
 E_\psi &= \frac{\partial}{\partial t} \left( \rho \left( e + \frac{|\mathbf{v}|^2}{2} + \frac{|\boldsymbol{\psi}|^2}{2} \right) \right) + \text{div} \left( \rho \mathbf{v} \left( e + \frac{|\mathbf{v}|^2}{2} + \frac{|\boldsymbol{\psi}|^2}{2} \right) + \Pi \mathbf{v} - \frac{1}{4\rho} w \mathbf{p} + \mathbf{A} \right) \\
 &= 0.
 \end{aligned}$$

The vector  $\mathbf{A}$  will be found later. Indeed,

$$\begin{aligned}
 E_\psi &= \rho \left( \dot{e} + \mathbf{v} \cdot \dot{\mathbf{v}} + \boldsymbol{\psi} \cdot \dot{\boldsymbol{\psi}} \right) + \text{div} \Pi \mathbf{v} + \text{tr} \left( \Pi \frac{\partial \mathbf{v}}{\partial \mathbf{x}} \right) - \frac{\mathbf{p}}{4\rho} \cdot \nabla w - \text{div} \left( \frac{\mathbf{p}}{4\rho} \right) w + \text{div} \mathbf{A} \\
 &= \rho \left( \dot{e} + \boldsymbol{\psi} \cdot \dot{\boldsymbol{\psi}} \right) + \text{tr} \left( \Pi \frac{\partial \mathbf{v}}{\partial \mathbf{x}} \right) - \frac{\mathbf{p}}{4\rho} \cdot \nabla w - \text{div} \left( \frac{\mathbf{p}}{4\rho} \right) w + \text{div} \mathbf{A} \\
 &= \rho \left( \dot{e} + \boldsymbol{\psi} \cdot \dot{\boldsymbol{\psi}} \right) + P \text{div} \mathbf{v} + \frac{1}{4\rho} \mathbf{p}^T \frac{\partial \mathbf{v}}{\partial \mathbf{x}} \mathbf{p} - \frac{\mathbf{p}}{4\rho} \cdot \nabla w - \text{div} \left( \frac{\mathbf{p}}{4\rho} \right) w + \text{div} \mathbf{A} \\
 &= \rho \left( \beta \dot{\eta} \ddot{\eta} + \frac{\dot{\rho}}{2} + \frac{1}{4} \frac{\mathbf{p}}{\rho} \cdot \left( \frac{\dot{\mathbf{p}}}{\rho} - \frac{\mathbf{p}}{\rho^2} \dot{\rho} \right) + \lambda \left( \frac{\eta}{\rho} - 1 \right) \left( \frac{\dot{\eta}}{\rho} - \frac{\eta}{\rho^2} \dot{\rho} \right) \right)
 \end{aligned}$$

$$\begin{aligned}
 & - \left( \frac{1}{2} \rho^2 - \frac{1}{4\rho} |\mathbf{p}|^2 + \lambda \eta \left( 1 - \frac{\eta}{\rho} \right) \right) \frac{\dot{\rho}}{\rho} + \frac{1}{4\rho} \mathbf{p}^T \frac{\partial \mathbf{v}}{\partial \mathbf{x}} \mathbf{p} - \frac{\mathbf{p}}{4\rho} \cdot \nabla w - \operatorname{div} \left( \frac{\mathbf{p}}{4\rho} \right) w \\
 & + \rho A_\psi \boldsymbol{\psi} \cdot \nabla \times \mathbf{p} + \operatorname{div} \mathbf{A} \\
 = & \rho A_\psi \boldsymbol{\psi} \cdot \nabla \times \mathbf{p} - \frac{A_p}{4\rho} \mathbf{p} \cdot \nabla \times \boldsymbol{\psi} + \operatorname{div} \mathbf{A}.
 \end{aligned}$$

Let us now take

$$\rho A_\psi = \frac{A_p}{4\rho} = \frac{a_c}{2} = \text{const} > 0.$$

Then

$$\begin{aligned}
 & \rho A_\psi \boldsymbol{\psi} \cdot \nabla \times \mathbf{p} - \frac{A_p}{4\rho} \mathbf{p} \cdot \nabla \times \boldsymbol{\psi} + \operatorname{div} \mathbf{A} \\
 = & \frac{a_c}{2} (\boldsymbol{\psi} \cdot \nabla \times \mathbf{p} - \mathbf{p} \cdot \nabla \times \boldsymbol{\psi}) + \operatorname{div} \mathbf{A} \\
 = & \frac{a_c}{2} \operatorname{div}(\mathbf{p} \times \boldsymbol{\psi}) + \operatorname{div} \mathbf{A}.
 \end{aligned}$$

Hence, it is sufficient to take  $\mathbf{A} = \frac{1}{2} a_c \boldsymbol{\psi} \times \mathbf{p}$  to have the energy conservation. Finally, in the thermodynamically compatible GLM cleaning procedure we must take

$$A_p = 2 a_c \rho, \quad A_\psi = \frac{a_c}{2\rho}, \quad a_c > 0.$$

In the main text we present this model also in coordinate form.

## References

1. Balsara, D., Käppeli, R., Boscheri, W., Dumbser, M.: Curl constraint-preserving reconstruction and the guidance it gives for mimetic scheme design. Communications in Applied Mathematics and Computational Science Submitted. [arxiv:2009.03522](https://arxiv.org/abs/2009.03522)
2. Barros, R., Gavriluk, S., Teshukov, V.: Dispersive nonlinear waves in two-layer flows with free surface. i. model derivation and general properties. Stud. Appl. Math. **119**, 191–211 (2007)
3. Bassi, C., Bonaventura, L., Busto, S., Dumbser, M.: A hyperbolic reformulation of the Serre–Green–Naghdi model for general bottom topographies. Comput. Fluids **212**, 104716 (2020)
4. Bassi, C., Busto, S., Dumbser, M.: High order ADER-DG schemes for the simulation of linear seismic waves induced by nonlinear dispersive free-surface water waves. Appl. Numer. Math. **158**, 236–263 (2020)
5. Bassi, F., Rebay, S.: A high-order accurate discontinuous finite element method for the numerical solution of the compressible Navier–Stokes equations. J. Comput. Phys. **131**, 267–279 (1997)
6. Baumann, C.E., Oden, T.J.: A discontinuous hp finite element method for the Euler and the Navier–Stokes equations. Int. J. Numer. Meth. Fluids **31**, 79–95 (1999)
7. Beji, S., Battjes, J.: Experimental investigation of wave propagation over a bar. Coast. Eng. **19**, 151–162 (1993)
8. Beji, S., Battjes, J.: Numerical simulation of nonlinear wave propagation over a bar. Coast. Eng. **23**, 1–16 (1994)
9. Bermúdez, A., Busto, S., Dumbser, M., Ferrín, J., Saavedra, L., Vázquez-Cendón, M.: A staggered semi-implicit hybrid FV/FE projection method for weakly compressible flows. J. Comput. Phys. **421**, 109743 (2020)
10. Bermudez, A., Vázquez-Cendón, M.: Upwind methods for hyperbolic conservation laws with source terms. Comput. Fluids **23**, 1049–1071 (1994)
11. Boscheri, W., Dumbser, M., Ioriatti, M., Peshkov, I., Romenski, E.: A structure-preserving staggered semi-implicit finite volume scheme for continuum mechanics. J. Comput. Phys. **2021**, 109866 (2010)
12. Boussinesq, J.: Théorie des ondes ed des remous qui se propagent le long d’un canal rectangulaire horizontal, en communiquant au liquide contenu dans ce canal des vitesses sensiblement pareilles de la surface au fond. Journal de Mathématiques Pures et Appliquées **17**, 55–108 (1872)

13. Bresch, D., Cellier, N., Couderc, F., Gisclon, M., Noble, P., Richard, G., Ruyer-Quil, C., Vila, J.: Augmented skew-symmetric system for shallow-water system with surface tension allowing large gradient of density. *J. Comput. Phys.* **419**, 109670 (2020)
14. Bresch, D., Couderc, F., Noble, P., Vila, J.: A generalization of the quantum Bohm identity: hyperbolic CFL condition for Euler–Korteweg equations. *C.R. Math.* **354**, 39–43 (2016)
15. Bresch, D., Gisclon, M., Lacroix-Violet, I.: On Navier–Stokes–Korteweg and Euler–Korteweg systems: application to quantum fluids models. *Arch. Ration. Mech. Anal.* **233**, 975–1025 (2019)
16. Briggs, M., Synolakis, C., Harkins, G., Green, D.: Laboratory experiments of tsunami runup on a circular island. *Pure Appl. Geophys.* **144**(3), 569–593 (1995)
17. Busto, S., Chiocchetti, S., Dumbser, M., Gaburro, E., Peshkov, I.: High order ADER schemes for continuum mechanics. *Front. Phys.* **8**, 32 (2020)
18. Busto, S., Ferrín, J., Toro, E.F., Vázquez-Cendón, M.E.: A projection hybrid high order finite volume/finite element method for incompressible turbulent flows. *J. Comput. Phys.* **353**, 169–192 (2018)
19. Busto, S., Tavelli, M., Boscheri, W., Dumbser, M.: Efficient high order accurate staggered semi-implicit discontinuous galerkin methods for natural convection problems. *Comput. Fluids* **198**, 104399 (2020)
20. Busto, S., Toro, E., Vázquez-Cendón, E.: Design and analysis of ADER-type schemes for model advection–diffusion–reaction equations. *J. Comput. Phys.* **327**, 553–575 (2016)
21. Castro, M., Gallardo, J., López, J., Parés, C.: Well-balanced high order extensions of Godunov’s method for semilinear balance laws. *SIAM J. Numer. Anal.* **46**, 1012–1039 (2008)
22. Castro, M., Gallardo, J., Parés, C.: High-order finite volume schemes based on reconstruction of states for solving hyperbolic systems with nonconservative products. Applications to shallow-water systems. *Math. Comput.* **75**, 1103–1134 (2006)
23. Castro, M., LeFloch, P., Muñoz-Ruiz, M., Parés, C.: Why many theories of shock waves are necessary: convergence error in formally path-consistent schemes. *J. Comput. Phys.* **227**, 8107–8129 (2008)
24. Castro, M.J., Fernández, E., Ferriero, A., García, J.A., Parés, C.: High order extensions of Roe schemes for two dimensional nonconservative hyperbolic systems. *J. Sci. Comput.* **39**, 67–114 (2009)
25. Cattaneo, C.: Sur une forme de l’équation de la chaleur éliminant le paradoxe d’une propagation instantanée. *Comptes Rendues de l’Académie des Sciences* **247**, 431–433 (1958)
26. Chesnokov, A., Liapidevskii, V.: Hyperbolic model of internal solitary waves in a three-layer stratified fluid. *Eur. Phys. J. Plus* **135**, 590 (2020)
27. Chiocchetti, S., Peshkov, I., Gavriluyk, S., Dumbser, M.: High order ADER schemes and GLM curl cleaning for a first order hyperbolic formulation of compressible flow with surface tension. *J. Comput. Phys.* **426**, 109898 (2021)
28. Cienfuegos, R., Barthélemy, E., Bonneton, P.: A fourth-order compact finite volume scheme for fully nonlinear and weakly dispersive Boussinesq-type equations. Part I: Model development and analysis. *Int. J. Numer. Methods Fluids* **51**, 1217–1253 (2006)
29. Cockburn, B., Hou, S., Shu, C.: The Runge–Kutta local projection Galerkin finite element method for conservation laws IV: the multidimensional case. *Math. Comput.* **54**, 545–581 (1990)
30. Cockburn, B., Lin, S.: TVB Runge–Kutta local projection discontinuous Galerkin finite element method for conservation laws III: one dimensional systems. *J. Comput. Phys.* **84**, 90–113 (1989)
31. Cockburn, B., Shu, C.: TVB Runge–Kutta local projection discontinuous Galerkin finite element method for conservation laws II: general framework. *Math. Comput.* **186**, 411–435 (1989)
32. Cockburn, B., Shu, C.: The Runge–Kutta local projection P1 discontinuous Galerkin method for scalar conservation laws. *Math. Modell. Numer. Anal.* **25**, 337–361 (1991)
33. Cockburn, B., Shu, C.W.: The local discontinuous Galerkin method for time-dependent convection diffusion systems. *SIAM J. Numer. Anal.* **35**, 2440–2463 (1998)
34. Cockburn, B., Shu, C.W.: Runge–Kutta discontinuous Galerkin methods for convection-dominated problems. *J. Sci. Comput.* **16**, 173–261 (2001)
35. Dedner, A., Kemm, F., Kröner, D., Munz, C.D., Schnitzer, T., Wesenberg, M.: Hyperbolic divergence cleaning for the MHD equations. *J. Comput. Phys.* **175**, 645–673 (2002)
36. Dell’Isola, F., Gavriluyk, S.: *Variational Models and Methods in Solid and Fluid Mechanics*. Springer, Berlin (2011)
37. Derigs, D., Winters, A.R., Gassner, G., Walch, S., Bohm, M.: Ideal GLM-MHD: about the entropy consistent nine-wave magnetic field divergence diminishing ideal magnetohydrodynamics equations. *J. Comput. Phys.* **364**, 420–467 (2018)
38. Dhaouadi, F., Favrie, N., Gavriluyk, S.: Extended Lagrangian approach for the defocusing nonlinear Schrödinger equation. *Stud. Appl. Math.* **207**, 1–20 (2018)
39. Diehl, D., Kremser, J., Kröner, D., Rohde, C.: Numerical solution of Navier–Stokes–Korteweg systems by Local Discontinuous Galerkin methods in multiple space dimensions. *Appl. Math. Comput.* **272**, 309–335 (2016)

40. Duchene, V.: Rigorous justification of the Favrie–Gavrilyuk approximation to the Serre–Green–Naghdi model. *Nonlinearity* **32**, 3772–3797 (2019)
41. Dumbser, M.: Arbitrary high order PNPM schemes on unstructured meshes for the compressible Navier–Stokes equations. *Comput. Fluids* **39**, 60–76 (2010)
42. Dumbser, M., Balsara, D., Toro, E., Munz, C.: A unified framework for the construction of one-step finite-volume and discontinuous Galerkin schemes. *J. Comput. Phys.* **227**, 8209–8253 (2008)
43. Dumbser, M., Castro, M., Parés, C., Toro, E.: ADER schemes on unstructured meshes for non-conservative hyperbolic systems: applications to geophysical flows. *Comput. Fluids* **38**, 1731–1748 (2009)
44. Dumbser, M., Enaux, C., Toro, E.: Finite volume schemes of very high order of accuracy for stiff hyperbolic balance laws. *J. Comput. Phys.* **227**, 3971–4001 (2008)
45. Dumbser, M., Facchini, M.: A local space-time discontinuous Galerkin method for Boussinesq-type equations. *Appl. Math. Comput.* **272**, 336–346 (2016)
46. Dumbser, M., Fambri, F., Gaburro, E., Reinartz, A.: On GLM curl cleaning for a first order reduction of the CCZ4 formulation of the Einstein field equations. *J. Comput. Phys.* **404**, 109088 (2020)
47. Dumbser, M., Peshkov, I., Romenski, E., Zanotti, O.: High order ADER schemes for a unified first order hyperbolic formulation of continuum mechanics: viscous heat-conducting fluids and elastic solids. *J. Comput. Phys.* **314**, 824–862 (2016)
48. Dumbser, M., Toro, E.F.: A simple extension of the Osher Riemann solver to non-conservative hyperbolic systems. *J. Sci. Comput.* **48**, 70–88 (2011)
49. Dumbser, M., Zanotti, O., Loubère, R., Diot, S.: A posteriori subcell limiting of the discontinuous Galerkin finite element method for hyperbolic conservation laws. *J. Comput. Phys.* **278**, 47–75 (2014)
50. Engsig-Karup, A., Hesthaven, J., Bingham, H., Warburton, T.: DG-FEM solution for nonlinear wave-structure interaction using Boussinesq-type equations. *Coast. Eng.* **55**, 197–208 (2008)
51. Escalante, C., Dumbser, M., Castro, M.: An efficient hyperbolic relaxation system for dispersive non-hydrostatic water waves and its solution with high order discontinuous Galerkin schemes. *J. Comput. Phys.* **394**, 385–416 (2019)
52. Escalante, C., Morales, T.: A general non-hydrostatic hyperbolic formulation for Boussinesq dispersive shallow flows and its numerical approximation. *J. Sci. Comput.* **83**, 62 (2020)
53. Escalante, C., de Luna, T.M., Castro, M.J.: Non-hydrostatic pressure shallow flows: GPU implementation using finite volume and finite difference scheme. *Appl. Math. Comput.* **338**, 631–659 (2018). <https://doi.org/10.1016/j.amc.2018.06.035>
54. Eskilsson, C., Sherwin, S.: An unstructured spectral/hp element model for enhanced Boussinesq-type equations. *Coast. Eng.* **53**, 947–963 (2006)
55. Eskilsson, C., Sherwin, S.: Spectral/hp discontinuous Galerkin methods for modelling 2D Boussinesq equations. *J. Comput. Phys.* **212**, 566–589 (2006)
56. Favrie, N., Gavrilyuk, S.: A rapid numerical method for solving Serre–Green–Naghdi equations describing long free surface gravity waves. *Nonlinearity* **30**, 2718–2736 (2017)
57. Gaburro, E., Castro, M.J., Dumbser, M.: Well-balanced Arbitrary-Lagrangian–Eulerian finite volume schemes on moving nonconforming meshes for the Euler equations of gas dynamics with gravity. *Mon. Not. R. Astron. Soc.* **477**(2), 2251–2275 (2018)
58. Gallardo, J., Parés, C., Castro, M.: On a well-balanced high-order finite volume scheme for shallow water equations with topography and dry areas. *J. Comput. Phys.* **227**, 574–601 (2007)
59. García-Navarro, P., Vázquez-Cendón, M.: On numerical treatment of the source terms in the shallow water equations. *Comput. Fluids* **29**, 951–979 (2000)
60. Godunov, S.: Symmetric form of the magnetohydrodynamic equation. *Numer. Methods Mech. Contin. Med.* **3**(1), 26–34 (1972)
61. Gottlieb, S., Shu, C.: Total variation diminishing Runge–Kutta schemes. *Math. Comput.* **67**, 73–85 (1998)
62. Green, A., Naghdi, P.: A derivation of equations for wave propagation in water of variable depth. *J. Fluid Mech.* **78**, 237–246 (1976)
63. Grosso, G., Antuono, M., Brocchini, M.: Dispersive nonlinear shallow-water equations: some preliminary numerical results. *J. Eng. Math.* **67**, 71–84 (2010)
64. Guermond, J., Popov, B., Tovar, E., Kees, C.: Robust explicit relaxation technique for solving the Green–Naghdi equations. *J. Comput. Phys.* **399**, 108917 (2019)
65. Hoefler, M., Ablowitz, M., Coddington, I., Cornell, E., Engels, P., Schweikhard, V.: On dispersive and classical shock waves in Bose–Einstein condensates and gas dynamics. *Phys. Rev. A* **74**, 023623 (2006)
66. Hyman, J., Shashkov, M.: Natural discretizations for the divergence, gradient, and curl on logically rectangular grids. *Comput. Math. Appl.* **33**, 81–104 (1997)

67. Jeltsch, R., Torrilhon, M.: On curl-preserving finite volume discretizations for shallow water equations. *BIT Numer. Math.* **46**, S35–S53 (2006)
68. Kazolea, M., Delis, A.I., Synolakis, C.E.: Numerical treatment of wave breaking on unstructured finite volume approximations for extended Boussinesq-type equations. *J. Comput. Phys.* **271**, 281–305 (2014). <https://doi.org/10.1016/j.jcp.2014.01.030>
69. LeVeque, R.J.: Balancing source terms and flux gradients in high-resolution Godunov methods: the quasi-steady wavepropagation algorithm. *J. Comput. Phys.* **146**, 346–365 (1998)
70. Levy, D., Shu, C., Yan, J.: Local discontinuous Galerkin methods for nonlinear dispersive equations. *J. Comput. Phys.* **196**, 751–772 (2004)
71. Lipnikov, K., Manzini, G., Shashkov, M.: Mimetic finite difference method. *J. Comput. Phys.* **257**, 1163–1227 (2014)
72. Luth, H., Klopman, B., Kitou, N.: Projects 13G: kinematics of waves breaking partially on an offshore bar; LDV measurements for waves with and without a net onshore current. Tech. rep., H1573, Delft Hydraulics, Delft, The Netherlands (1994)
73. Lynett, P., Liu, P.: A two-layer approach to wave modelling. *Proc. Roy. Soc. Lond. Ser. A: Math., Phys. Eng. Sci.* **460**(2049), 2637–2669 (2004)
74. Lynett, P., Wu, T., Liu, P.F.: Modeling wave runup with depth-integrated equations. *Coast. Eng.* **46**(2), 89–107 (2002)
75. Madelung, E.: Quantentheorie in hydrodynamischer form. *Zeitschrift für Physik* **40**, 322–326 (1927)
76. Madsen, P., Murray, R., Sørensen, O.: A new form of the Boussinesq equations with improved linear dispersion characteristics. *Coast. Eng.* **15**, 371–388 (1991)
77. Madsen, P., Sørensen, O.: A new form of the Boussinesq equations with improved linear dispersion characteristics. Part 2. A slowly varying bathymetry. *Coast. Eng.* **18**, 183–204 (1992)
78. Maso, G.D., LeFloch, P., Murat, F.: Definition and weak stability of nonconservative products. *J. Math. Pures Appl.* **74**, 483–548 (1995)
79. Mazaheri, A., Ricchiuto, M., Nishikawa, H.: A first-order hyperbolic system approach for dispersion. *J. Comput. Phys.* **321**, 593–605 (2016)
80. Montecinos, G., Toro, E.: Reformulations for general advection–diffusion–reaction equations and locally implicit ad schemes. *J. Comput. Phys.* **275**, 415–442 (2014)
81. Muñoz, M., Parés, C.: Godunov method for nonconservative hyperbolic systems. *Math. Modell. Numer. Anal.* **41**, 169–185 (2007)
82. Müller, I., Ruggeri, T.: *Rational Extended Thermodynamics*. Springer, Berlin (1998)
83. Munz, C., Omnes, P., Schneider, R., Sonnendrücker, E., Voss, U.: Divergence correction techniques for Maxwell solvers based on a hyperbolic model. *J. Comput. Phys.* **161**, 484–511 (2000)
84. Nishikawa, H.: A first-order system approach for diffusion equation. I: second-order residual-distribution schemes. *J. Comput. Phys.* **227**(1), 315–352 (2007)
85. Nishikawa, H.: A first-order system approach for diffusion equation. II: unification of advection and diffusion. *J. Comput. Phys.* **229**(11), 3989–4016 (2010)
86. Parés, C.: Numerical methods for nonconservative hyperbolic systems: a theoretical framework. *SIAM J. Numer. Anal.* **44**, 300–321 (2006)
87. Peregrine, D.: Long waves on a beach. *J. Fluid Mech.* **27**, 815–827 (1967)
88. Peshkov, I., Romenski, E.: A hyperbolic model for viscous Newtonian flows. *Contin. Mech. Thermodyn.* **28**, 85–104 (2016)
89. Rhebergen, S., Bokhove, O., van der Vegt, J.: Discontinuous Galerkin finite element methods for hyperbolic nonconservative partial differential equations. *J. Comput. Phys.* **227**, 1887–1922 (2008)
90. Ricchiuto, M., Filippini, A.: Upwind residual discretization of enhanced Boussinesq equations for wave propagation over complex bathymetries. *J. Comput. Phys.* **271**, 306–341 (2014)
91. Roeber, V., Cheung, K.F., Kobayashi, M.H.: Shock-capturing Boussinesq-type model for nearshore wave processes. *Coast. Eng.* **57**(4), 407–423 (2010). <https://doi.org/10.1016/j.coastaleng.2009.11.007>
92. Romenski, E.: Hyperbolic systems of thermodynamically compatible conservation laws in continuum mechanics. *Math. Comput. Modell.* **28**(10), 115–130 (1998)
93. Seabra-Santos, F.J., Renouard, D.P., Temperville, A.M.: Numerical and experimental study of the transformation of a solitary wave over a shelf or isolated obstacle. *J. Fluid Mech.* **176**, 117–134 (1987)
94. Serre, F.: Contribution à l'étude des écoulements permanents et variables dans les canaux. *Houille Blanche* **8**, 374–388 (1953)
95. Synolakis, C.E.: The runup of solitary waves. *J. Fluid Mech.* **185**, 523–545 (1987). <https://doi.org/10.1017/S002211208700329X>
96. Titarev, V., Toro, E.: ADER: arbitrary high order Godunov approach. *J. Sci. Comput.* **17**(1–4), 609–618 (2002)

97. Titarev, V., Toro, E.: ADER schemes for three-dimensional nonlinear hyperbolic systems. *J. Comput. Phys.* **204**, 715–736 (2005)
98. Toro, E.: *Riemann Solvers and Numerical Methods for Fluid Dynamics*, 2nd edn. Springer, Berlin (1999)
99. Toro, E., Montecinos, G.: Advection-diffusion-reaction equations: hyperbolization and high-order ADER discretizations. *SIAM J. Sci. Comput.* **36**, A2423–A2457 (2014)
100. Toro, E., Titarev, V.: Solution of the generalized Riemann problem for advection–reaction equations. *Proc. Roy. Soc. Lond.*, 271–281 (2002)
101. Toro, E.F., Titarev, V.A.: Derivative Riemann solvers for systems of conservation laws and ADER methods. *J. Comput. Phys.* **212**(1), 150–165 (2006)
102. Treske, A.: Undular bores (Favre-waves) in open channels-experimental studies. *J. Hydraul. Res.* **32**, 355–370 (1994)
103. van Leer, B.: Towards the ultimate conservative difference scheme V: a second order sequel to Godunov’s method. *J. Comput. Phys.* **32**, 101–136 (1979)
104. Vázquez-Cendón, M.: Improved treatment of source terms in upwind schemes for the shallow water equations in channels with irregular geometry. *J. Comput. Phys.* **148**, 497–526 (1999)
105. Yamazaki, Y., Kowalik, Z., Cheung, K.: Depth-integrated, non-hydrostatic model for wave breaking and run-up. *Numer. Methods Fluids* **61**, 473–497 (2008)
106. Yan, J., Shu, C.: A local discontinuous Galerkin method for KdV type equations. *SIAM J. Numer. Anal.* **40**, 769–791 (2002)
107. Yan, J., Shu, C.: Local discontinuous Galerkin methods for partial differential equations with higher order derivatives. *J. Sci. Comput.* **17**, 27–47 (2002)
108. Zanotti, O., Fambri, F., Dumbser, M., Hidalgo, A.: Space-time adaptive ADER discontinuous Galerkin finite element schemes with a posteriori sub-cell finite volume limiting. *Comput. Fluids* **118**, 204–224 (2015)

**Publisher’s Note** Springer Nature remains neutral with regard to jurisdictional claims in published maps and institutional affiliations.